Study of a Heavy Rain Vortex Formed over the Eastern Flank of the Tibetan Plateau

BIN WANG*

Geophysical Fluid Dynamics Program, Princeton University, Princeton, NJ 08542

ISIDORO ORLANSKI

Geophysical Fluid Dynamics Laboratory/NOAA, Princeton University, Princeton, NJ 08542

(Manuscript received 15 September 1986, in final form 3 January 1987)

ABSTRACT

A case of the heavy rain vortex which occurred during the period 14–15 July 1979 is studied using a limited-area mesoscale numerical model. This is a representative example of a group of warm southwest vortices that often form over the eastern flank of the Tibetan Plateau after the onset of the summer Indian monsoon.

Some common features of the dynamic structures exhibited both by the simulation and by observations are discussed. The developing vortex is noticeably detached from the polar frontal zone. A 180° phase shift exists between the upper and lower layer vorticity fields. In the boundary layer, a pronounced northward transport of mass and moisture is connected with an intense upward motion near and to the east of the 700-mb vortex center, while the southward cold advection is insignificant.

The vortex originated and rapidly developed in a stagnation region on the lee side of the plateau. The presence of the stagnation region not only removes local dynamical energy sources from the environmental flow, but also diminishes topographic generation of vorticity by reducing the vortex stretching in the wind component flowing over the plateau and the horizontal convergence in the component moving around the plateau. Without latent heating, dynamic instability and/or forcing of the large-scale flow interacting with the Tibetan Plateau is not sufficient to generate the observed disturbance.

On the other hand, the plateau blocking effect favors the establishment of a conditionally unstable environment. The simulation indicates that a sudden onset of vigorous deep convection, followed by a rapid growth of relative vorticity in the lower troposphere, takes place once the dynamic forcing associated with a mesoscale plateau disturbance was positioned over the western stagnation region. Our principle result is that the warm heavy rain vortex in this case study is triggered by a migratory plateau boundary layer disturbance and basically driven by cumulus convective heating. The thermal influence of the elevated plateau topography may appreciably affect the vortex initiation through changing the intensity of the forcing associated with the triggering mechanism.

1. Introduction

This study is concerned with the dynamics of a heavy rain vortex that formed over the eastern flank of the Tibetan (Qinghai-Xizang) Plateau. This type of vortex is important in the summer Asian monsoon circulation because of its large rainfall rate and because it represents a manifestation of the dynamic and thermal influences of the Tibetan Plateau.

Customarily, Chinese meteorologists refer to the vortices developing over the eastern flank of the plateau as southwest vortices (referred to here as SW vortices), because they commonly originate in the Sichuan Basin and its neighborhood in southwest China (Fig. 1). These vortices have a typical horizontal dimension of 500–1000 km. Their cyclonic circulation is primarily confined to the lower troposphere and is most clearly identified on a 700-mb weather map during their developing period. When moving eastward or east-northeastward, they frequently cause surface cyclogenesis and produce heavy rainfall over a widespread downstream region. For instance, a climatological study has shown that nearly two-thirds of the total number of SW vortices, which occurred during April through July of 1970–74, cause heavy rainfall along the middle Yangzi River Valley (Tao et al., 1980).

The Tibetan Plateau is not only a huge blocker, but also a vast heat source during the summer. As a consequence, the monthly mean charts for July show that, at 500 mb a thermal low occupies the plateau region, while at the upper troposphere, a planetary Tibetan High dominates the circulation. The circulation around the plateau is quite different from that favorable for lee cyclogenesis. First, on the lee side of the plateau the baroclinicity is rather weak in the middle and lower troposphere. Second, the lower tropospheric flow, which tends to move along the topographic contour, is decoupled with the middle tropospheric flow which moves over the plateau; consequently the vorticity stretching effect on the lee side is very weak. Finally, the middle tropospheric disturbances are usually rather

* Present affiliation: Department of Meteorology, University of Hawaii, Honolulu, HI 96822.

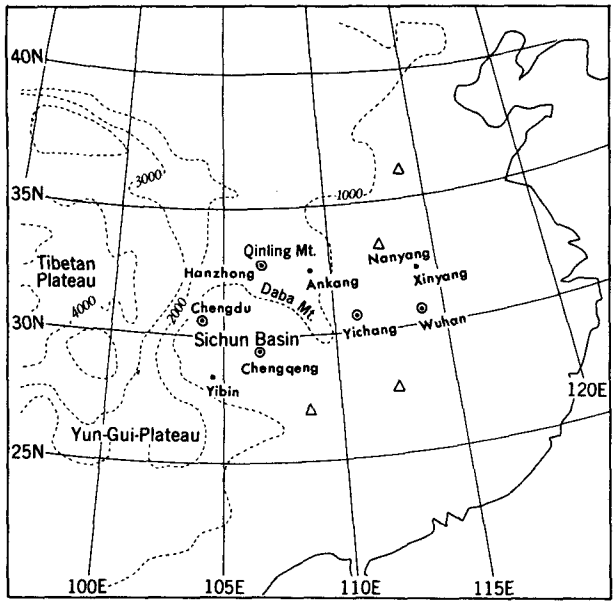

FIG. 1. Map of model domain (28 × 28) with contours indicating height above sea level, in meters, of the actual terrain. Circles and triangles indicate the locations where the temperatures are sampled (section 4).

weak and confined only to the plateau boundary layer. These climatological conditions seem to indicate that the vortex-genesis on the lee side of the plateau in the summer differs from the classical view of the lee cyclogenesis.

The development of SW vortices, of course, is closely related to the seasonal variations in the large-scale circulation over East Asia, which is, to a great extent, affected by the thermal and mechanical forcings of the Tibetan Plateau. Since there is a large seasonal component to the East Asian circulation, it is expected that the generation and intensification of SW vortices exhibit different characteristics in different seasons. Some of them occur prior to the commencement of Mei-yu (plum rain) in the Yangzi river and Indian summer monsoon; these may be identified as baroclinic systems associated with cold air intrusion of the polar front. Others are often observed after the westerly jet stream has shifted to the north of the plateau; these are formed in a region relatively far away from baroclinic frontal zone and are referred to as warm SW vortices (e.g., Luo, 1979). In this study a warm SW vortex and associated heavy rainfall will be discussed.

Our major concerns in understanding the dynamics of the warm SW vortices involve at least two important aspects: first, the direct influences of the world's highest plateau on the genesis of these mesoscale vortices, and, second, the role of convective latent heating in the generation and intensification of these vortices. Numerical experiments will be performed in order to elucidate the complicated physical processes involving the influences of the Tibetan Plateau and diabatic heating.

Two numerical studies with contrasting results have recently been reported concerning the same catastrophic flooding in the Sichuan province that occurred on 11–15 July 1981 (Hovermale, 1983; Chen and Dell'Osso, 1984). This flooding event was caused by a warm SW vortex and was characterized by extensive mesoscale convective development. The results of Chen and Dell'Osso suggest that the vortex was initiated over the interior region of the plateau and intensified over its eastern boundary with the release of latent heat playing an important part. Hovermale's results, however, suggest that the vortex formed along the eastern boundary of the plateau, as defined by the 3000-m isohypse, no matter whether latent heating was included or not. Thus far, the physical processes responsible for the initiation and intensification of these warm heavy rain vortices are not well understood. In particular, the way in which the Tibetan Plateau influences their development needs to be further clarified.

The major purpose of the present numerical study is to identify the principal physical mechanisms which may be responsible for the development of an observed warm SW vortex. More specifically, we shall be concerned with the effects of latent heat release and the influence of the Tibetan Plateau on vortex formation. This particular vortex has been selected because it is typical of summer disturbances in this region and because 1979 was the FGGE year during which a coherent dataset for the global circulation is available. Details of the vortex event are reviewed in section 2. Section 3 briefly describes the numerical model used in this study. Section 4 provides a discussion of difficulties encountered in the analyzed ECMWF/FGGE dataset and the way in which the data were modified to correct this problem. In sections 5–7 we display the dynamic structure and evolution of the vortex, as well as analyze the impact of latent heat release and changes in the surface heat flux and mechanical forcing of the plateau on the model simulations.

2. Synoptic conditions and the vortex events

During 14–15 July 1979, a cyclonic vortex formed over the northeastern Sichuan Basin and rapidly developed as it moved east-northeastward between 33° and 35°N toward the Henan province. Figure 2a shows a subjective analysis of the 700-mb geopotential height and wind fields at 0000 UTC 15 July when the identifiable cyclonic circulation first occurred. The vortex, whose center is located near Ankang (32.5°N, 109°E), is associated with a southwest–northeast shear line and has an asymmetric structure: strong southwest wind to the southeast, and relatively weak northerly flow to the northwest of the vortex. The consecutive positions of the 700-mb maximum vorticity derived from ECMWF FGGE analysis are indicated by circles in Fig. 2b. The solid curves are contours of precipitation in units of millimeters, showing the precipitation of the 24-h pe-

700mb GEOPOTENTIAL

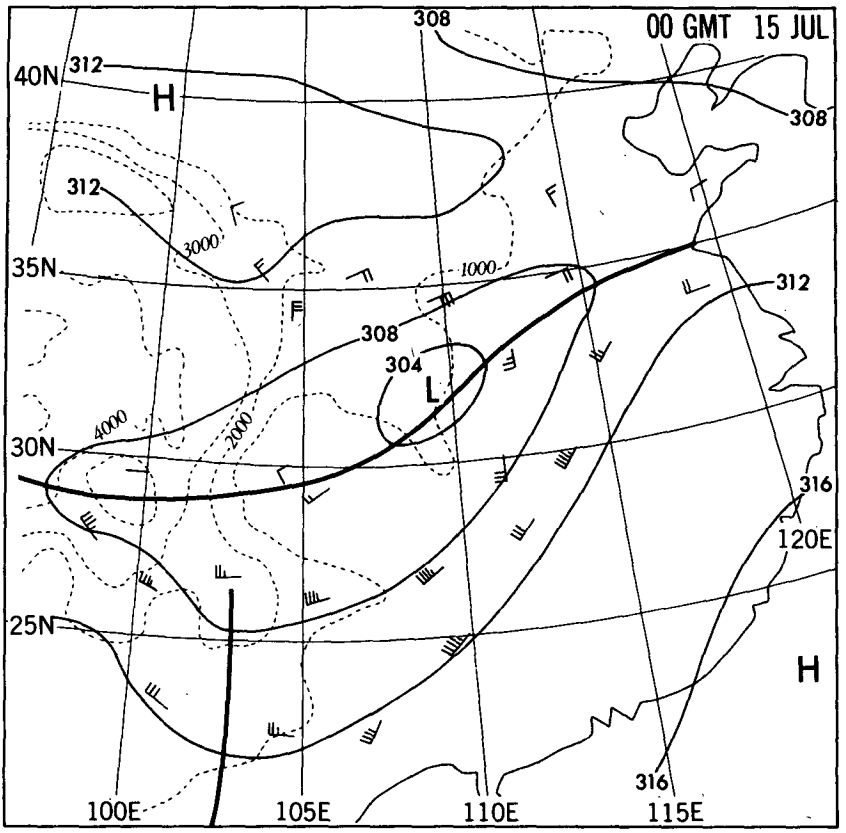

24hr PRECIPITATION

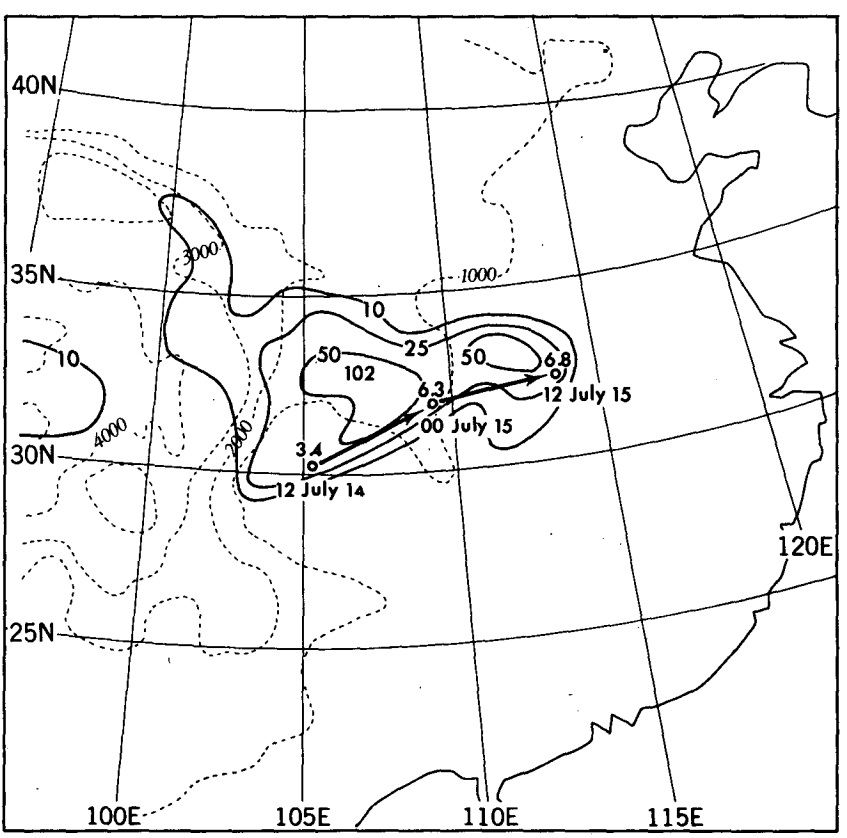

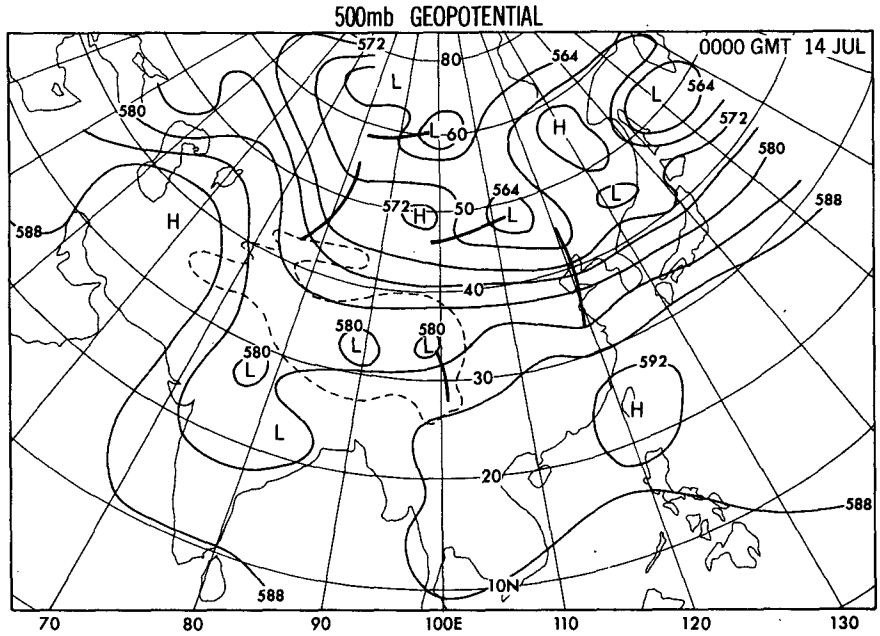

FIG. 3. Five hundred mb geopotential height chart of 0000 UTC 14 July 1979. The dashed curve is the terrain contour of 3000 m above sea level, indicating the main body of the Tibetan Plateau.

riod from 0000 UTC 14 July to 0000 UTC 15 July. The maximum precipitation in excess of 100 mm occurred near Hanzhong (south of the Qinling Mountain) and Nanyang. Heavy rainfall continued to spread over the downstream region as the vortex moved eastward after 0000 UTC 15 July. One of the most striking features of this scenario is that the formation of the vortex circulation was accompanied by intensive convective rainfall.

At the beginning of the period (0000 UTC 14 July), several characteristic features may be noted from the 500-mb geopotential map shown in Fig. 3. Very impressive is the abnormal development of the Western Pacific subtropical high (WPSH) (note the 5880 m contour of geopotential height in Fig. 3), which elongated in the zonal direction and extended westward to 97°E, more than 15° farther than normal. The eastern flank of the plateau is thus located at the northwest edge of the WPSH. This is usually a significant precursor of heavy precipitation. Second, a nearly east–west oriented polar frontal zone and the associated jet stream is observed in the middle latitudes between 40° and 45°N ahead of the Iran High. We note that the main baroclinic zone at 500 mb remained north of 37°N during the entire period of interest, implying that the heavy rainfall vortex was formed within a relatively uniform warm and moist air mass. Last, the region over the Tibetan Plateau and north India was covered by a broad trough with several low systems in it. Our period of interest begins after 5–15 mm of precipitation has been deposited over a portion of the southeastern plateau and after a mesoscale low that had formed 12 h earlier has moved to the eastern plateau around (97°E, 33°N). Whether or not this disturbance moved off the plateau seems to have considerable importance to the development of the warm SW vortex.

At 700 mb, a dominant feature is the confluence of two branches of the westerly flow, which were deflected by the main body of the plateau in an upstream region, east of 115°E, about 1200 km away from the eastern edge of the plateau as defined by the 3000 m isohypse (Fig. 4a). A noticeable wake, in which the horizontal motion of the air is much weaker than in the surrounding region, exists on the lee side of the plateau. This low-wind or stagnation region, affected by the elevated surface heating, may be regarded as a part of the Tibetan Plateau monsoon region (Gao et al., 1981). It is in this low-wind region that a cyclonic vortex originated and intensified rapidly during the ensuing 24 hours. The vorticity field at 700 mb (Fig. 5a) shows a cyclonic

FIG. 2. (a) Seven hundred mb subjective analysis for 0000 UTC 15 July 1979. A full wind barb denotes 4 m s^{-1}. (b) Observed accumulated precipitation (mm) for 24-hour period from 0000 UTC 14 July to 0000 UTC 15 July 1979 and successive positions of the 700-mb vorticity center indicated by the circles. The numbers above the circles are maximum vorticity in units of 10^{-5} s^{-1}.

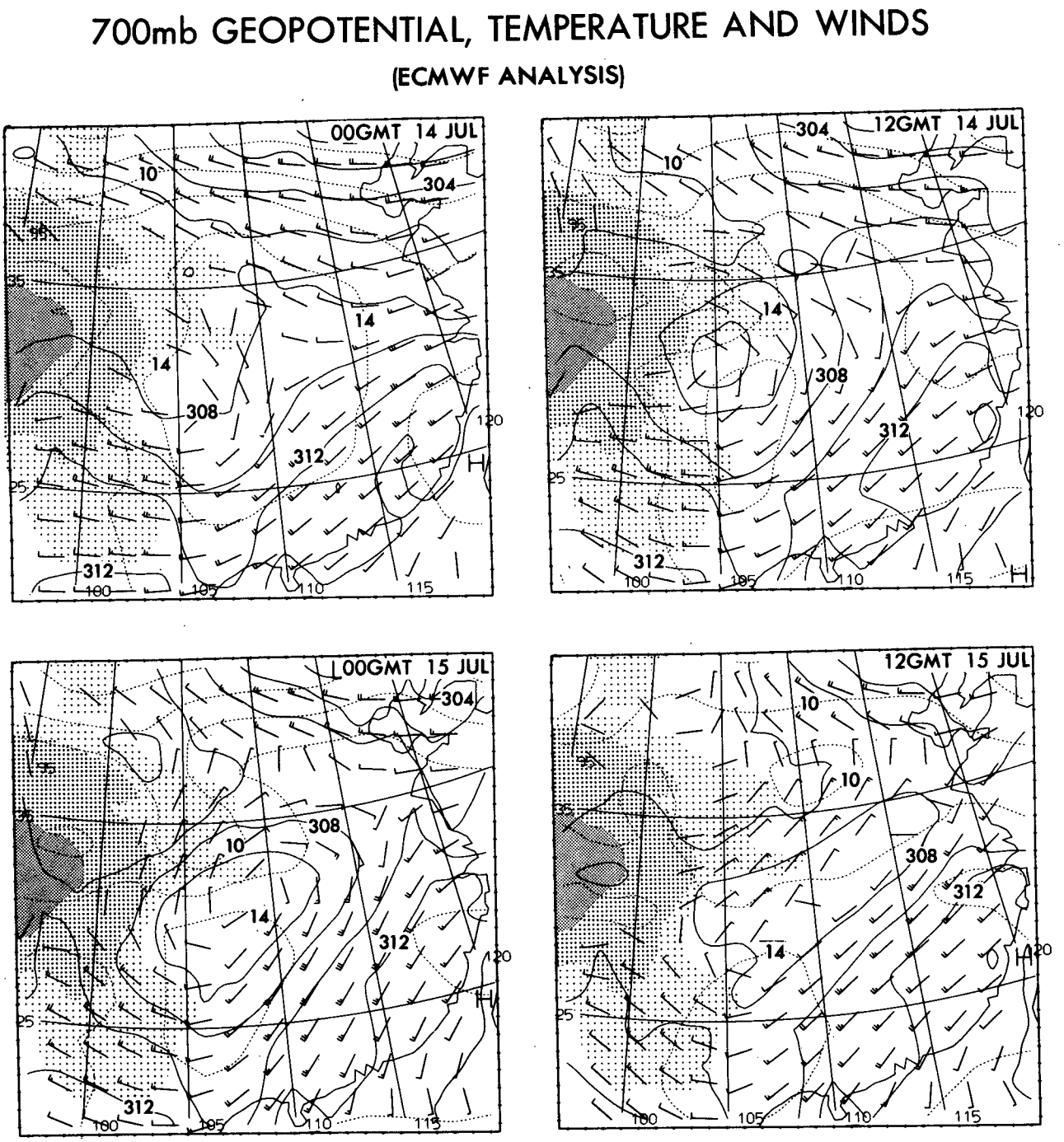

FIG. 4. Plots of 700-mb wind, geopotential height (solid curve in units of 10 m), and temperature (dotted contour in units of °C) fields analyzed from ECMWF/FGGE data for (a) 0000 UTC, (b) 1200 UTC 14 July, (c) 0000 UTC, and (d) 1200 UTC 15 July 1979. Tick marks in both zonal and meridional are in 96-km increments. A full wind bar represents 5 m s^{-1}. The light, moderate and dark shadings denote, respectively, the region where 1500 m $\leq h <$ 3000 m, 3000 m $\leq h <$ 4500 m and $h >$ 4500 m, h being the topographic height above the sea level.

vorticity region around the southeastern edge and an anticyclonic vorticity region with an almost equal strength around the northeastern edge of the plateau. This vorticity pattern is mainly attributed to the curvatures and horizontal shears of the two branches of the confluent flow.

By 1200 UTC 14 July, a low-pressure zone appeared at 700 mb over the Sichuan Basin around (31°N,

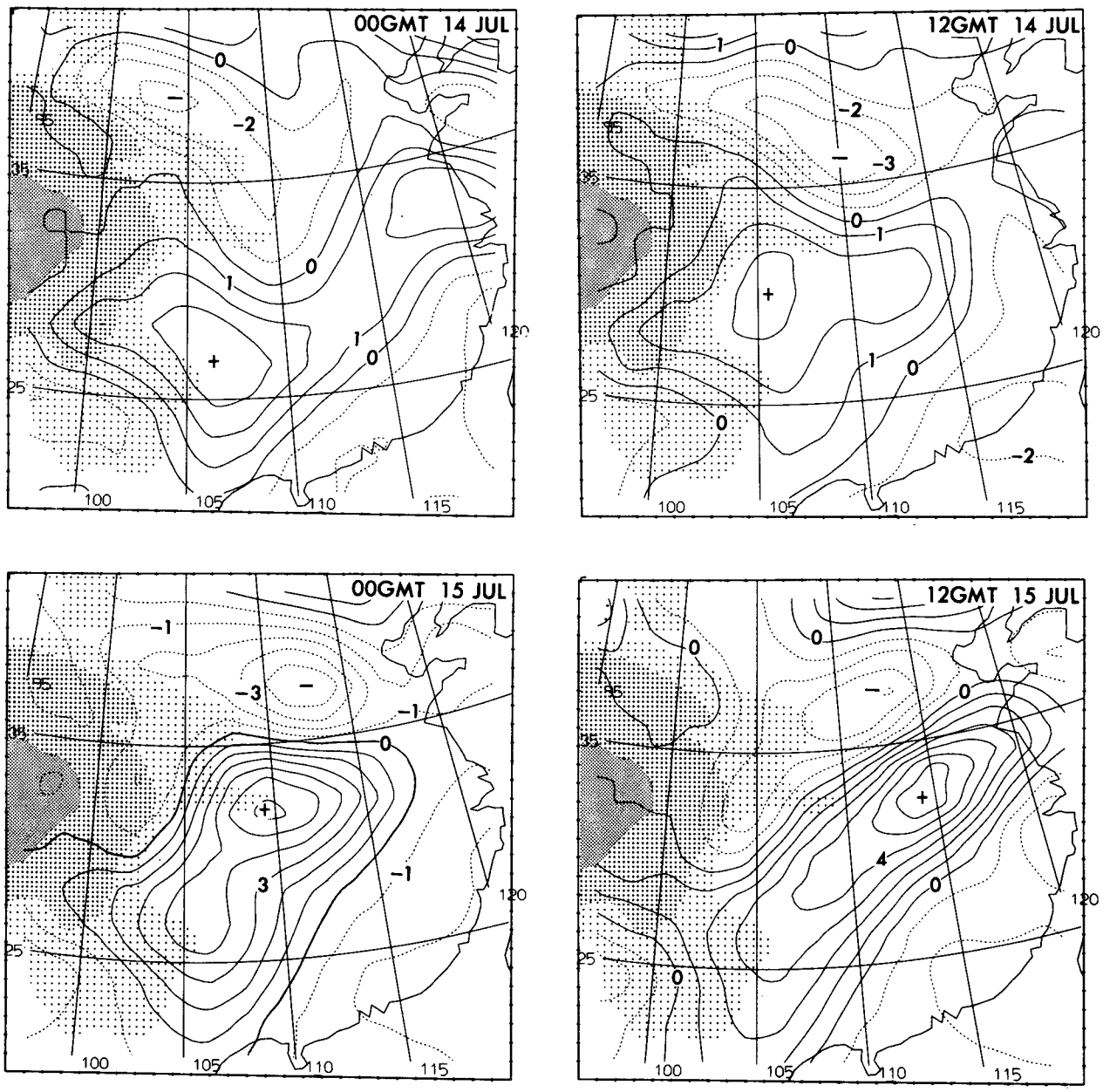

FIG. 5. As in Fig. 4 except for the relative vorticity (10^{-5}) field.

105°E) with an ageostrophic southeast wind component to the north and warm advection to the east of the low (Fig. 4b). A noteworthy feature is the absence of any significant cold advection in the vicinity of the incipient low. At the corresponding 500-mb level, the positive vorticity center associated with the plateau boundary layer disturbance had moved to the plateau edge near (33.5°N, 102°E), and its central vorticity had increased slightly from (3.2 to 4.4) $\times 10^{-5}$ s^{-1} (refer to Fig. 7).

In the following 12 h, the cyclonic vorticity rapidly increased and a well-defined cyclonic circulation appeared on the northeastern side of the Daba Mountain (near Ankang), where the topographic height is around 1500 m (Figs. 4c and 5c). An enhanced low-level southwest jet is seen between the vortex and the

WPSH with a speed reaching 15 m s^{-1}. This low-level jet extends downward to 850 mb (not shown). The strengthening of the vortex induced a change in the wind direction at its rear flank from easterly to northerly; meanwhile a localized "cold wedge" appeared in the northwestern part of the vortex. It is important to point out that, by the time an identifiable SW vortex is evident (0000 UTC 15 July), over 100 mm of rain has already been deposited near the vortex center. In fact, this behavior often makes timely forecasting impossible.

From 0000 UTC through 1200 UTC 15 July, there is a stretching of the cyclonic circulation in the southwest–northeast direction (Fig. 4d), with the main positive vorticity center moving to the north of Xienyang (32.5°N, 114°E) without any appreciable change in its intensity (Fig. 5d). However, the corresponding 500-mb trough filled rapidly; meanwhile, the maximum vorticity associated with the vortex seems to extend downward from 700 to 850 mb following the topographic features, and a weak surface cyclone developed at 1200 UTC 15 July in the front of the 700-mb vortex near (32.5°N, 115°E). The average translation speed of the vortex during 1200 UTC 14 July to 1200 UTC 15 July was about 9° longitude per day.

3. Brief description of the model

The numerical model employed in the present study is a primitive equation model applied to a limited area with 17 equally spaced layers in a z-coordinate. The model is 15 km deep with a rigid lid at the top. The horizontal domain contains 28 points in both the zonal and meridional directions with a grid size of 96.5 km. The integration time step is 2 minutes. The model characteristics have been described at length by Ross and Orlanski (1982) except for the inclusion of a parameterization of the topographical effects.

To simulate the generation of SW vortices which formed over the eastern slope of the Tibetan Plateau, a mesoscale model domain must include at least a portion of the main body of the plateau. The topography used in the present numerical simulations was interpolated from a 1/6 degree latitude by 1/6 degree longitude NCAR grid terrain data using a 16-point Bessel interpolation scheme. The highest altitude of the topography within the domain is over 5500 m, and the steepest slope of the plateau periphery is roughly 1:50 (Fig. 1). The results from numerical experiments undertaken by Wu and Chen (1985) suggest that the smoothing of topography by reducing mountain height and expanding mountain area in a numerical simulation of the SW vortex may result in serious inaccuracy in the predicted vortex location. It was also recognized that, in a region of steep orographic slope, the use of a σ-coordinate may cause interpolation errors of geopotential height gradients (Mesinger, 1982). An alternate approach has been developed and tested by Orlanski and Polinsky (1984) in which the mechanical influence of orography is simulated by a "viscous fluid mountain." In this technique, a large body drag term with the shape of the mountain is incorporated into the model's momentum equations. This procedure effectively diminishes the wind velocity inside the mountain configuration to very small values. At the surface of the orographic features, the mountain body drag reduces to a specified surface drag. The horizontal velocity is calculated in the middle of each layer from z_0 to $z_0 + \Delta z$; hence, if the topographic height is between the values of two adjacent grid levels, i.e., $z_0 \leqslant h < z_0 + \Delta z$, the body drag for this layer is simply assumed to increase with the distance $(h - z_0)$. A momentum budget for a vertical air column from the model upper boundary to the orographic surface leads to the following expression for the mountain viscous stress:

$$\tau_m(h) = \left(\frac{\delta}{1-\delta}\right)\rho C_D|\mathbf{v}|\mathbf{v}, \tag{3.1}$$

where C_D is the surface drag coefficient (a value of 1.25×10^{-3} is used in this study), ρ is the air density, $\mathbf{v}$ the horizontal wind vector, and

$$\delta = \min\left[\frac{h - z_0}{\Delta z}, \delta_{\max}\right], \quad \delta_{\max} < 1, \tag{3.2}$$

i.e., δ is determined by the minimum of the two terms in the brackets of (3.2). Thus, for an underground layer, the stress is given by (3.1) with $\delta \equiv \delta_{\max}$. In the present study, $\delta_{\max}$ is assumed to be 0.99583. This simple scheme has the following virtues: 1) z is kept as a vertical coordinate and the levels are horizontal; 2) the steep viscous mountain tends to simulate reasonably well the mechanical effects of blocking and the surface drag due to the existence of the mountain.

Although the radiative heating at the surface was neglected, the sensible and latent heat fluxes at the mountain surface have been included in the model. They are assumed to be proportional to the temperature and moisture gradients, respectively. These surface fluxes are produced primarily by the vertical eddy diffusivity in the model. Because the large viscosity within the mountain configuration dramatically suppresses the motion inside the mountain, the vertical motion across the terrain surface is extremely small. Thus the heat and moisture fluxes are not appreciable affected by this approximate lower boundary condition at the model terrain surface.

Another feature of interest is that the cumulus convective heating is not parameterized in terms of any closure assumption; rather, it is taken into account in the thermodynamic equation as a result of "resolvable" scale supersaturation (the so-called explicit representation). Any water vapor in excess of an effective saturation mixing ratio, kq_s, immediately condenses out, where k is the effective saturation relative humidity at which condensation is assumed to occur within each

grid box. Since convective precipitation may take place before the area-averaged saturation in a mesoscale grid box is reached, the value of k should be less than 1 (Smagorinsky, 1960). In view of the current model resolution of 96.5 km, the factor k is set to 0.85. A prognostic equation for condensed water is also included in the model [see Eq. (2.6) of Ross and Orlanski, 1984], so that condensation produces cloud water which is advected and diffused horizontally and vertically. When cloud water content exceeds a threshold value, C_r, the excessive cloud water is assumed to precipitate immediately and is removed from the atmospheric column without consideration of evaporation of raindrops in the lower, unsaturated layers. A negative buoyancy of cloud water loading, which opposes excessive updraft development at a single grid point, is also incorporated into the hydrostatic equation. The value for the threshold of the cloud water loading, C_r, is 1.5 g m^{-3}, the same as that used in several previous studies (e.g., Ross and Orlanski, 1982). In view of the fact that latent heat released in a meso-alpha scale model can be excessive in the treatment of explicit convection (Ross and Orlanski, 1982), a cloud fraction function, C_F, which is, in general, a function of height, was introduced into the latent heating terms in the thermodynamic equation to modify the amount of latent heat released at different levels. The function C_F may be thought of as the vertical distribution of fractional cloud coverage in a grid column of horizontal area $(\Delta x)^2$. Since the elevation of the surface in our model domain exhibits large horizontal variations (from over 5000 m down to sea level), so does the height of the cloud base; we, therefore, simply assume that the cloud fraction is a constant value of 0.85 for the present model resolution.

For grid sizes of less than a few kilometers, the explicit convective scheme will explicitly resolve cumulus convective cloud elements, and more relevant cloud physics can be incorporated into such a model. However, in a meso-alpha or meso-beta scale model with a grid resolution of 20–150 km, this scheme cannot resolve individual cumulus clouds; rather, it produces a model cloud which essentially parameterizes effects of cumulus heating with a dynamical interaction between the model clouds and the mesoscale motion. The introduction of grid size-dependent parameters, such as the effective saturation relative humidity, the rainwater autoconversion threshold, and the cloud fraction function, reflects the philosophy behind this scheme. It should be also pointed out that the present model treats the effects of cumulus convection on the grid scale by using the eddy viscosity and diffusivity, which are nonlinear functions of the bulk Richardson number (Ross and Orlanski, 1982). These eddy viscosity and diffusivity gradually adjust any unstable saturated air to a neutral state as the model convection develops. This type of heating scheme has been successfully used in meso-beta scale models with grid sizes ranging from 20 km (Ross, 1986) to 60 km (Orlanski and Ross, 1984). We now apply it to a meso-alpha scale model with a grid size of 96 km. A comparative experiment with grid size of 69 km has also been carried out. The results are similar to those obtained from the 36-hour simulation using 96-km grid resolution. It is our belief that the "explicit" representation of cumulus heating effects is quite competitive with other cumulus parameterization schemes, such as convective adjustment (Manabe et al., 1965), the Kuo and the Arakawa–Schubert cumulus parameterization schemes in a mesoscale model.

4. Simulation with FGGE IIIb dataset

In view of the scarcity of observed data over the Tibetan Plateau, especially the western plateau, we have located the model's upstream boundary across the eastern plateau around 95°E (Fig. 1), where observations are relatively dense. Both the GFDL and ECMWF FGGE IIIb datasets are used to initialize the model at 0000 UTC 14 July and to provide time-dependent boundary conditions for 36-hour simulations. It was found that the upper tropospheric (250 mb) temperature field from the GFDL/FGGE dataset exhibits unrealistically large horizontal gradients and an excessively strong easterly jet over the southern periphery of the plateau. Since the open boundary condition requires the total column convergence to vanish, the exaggerated upper easterly jet causes extraordinarily intense westerly inflow at the lower levels. This inaccuracy in the upstream low-level flow moving around the plateau in turn induces large distortion in the simulated solutions for this case. Thus the simulation was carried out using ECMWF dataset, which provides better upstream conditions. However, this dataset also has deficiencies which will be discussed here.

Figure 6 shows the simulated 700-mb geopotential height, wind and temperature at hour 24 using original ECMWF/FGGE data for initial and boundary conditions. A weak cyclonic circulation is seen near (34°N, 106°E) about 300 km to the northwest of the observed position, with a vorticity intensity less than half the observed value. This transforms into a southwest–northeast shear line in the following 12 hours. The maximum 24-hour precipitation by 0000 UTC 15 July is only 10 mm, occurring near (35°N, 107°E). Overall, the simulated solution is somewhat similar to the observed case but far from satisfactory.

Examination of the original ECMWF/FGGE data analysis reveals that the temperature field below 2 km has systematic biases: there is a strong temperature inversion layer that spreads over almost the whole domain and persists for the entire period of interest. This inversion tends to reduce thermodynamic and dynamic instabilities and the amount of precipitation, thus significantly suppressing the development of the vortex. Figures 8a and 8b compare vertical temperature dis-

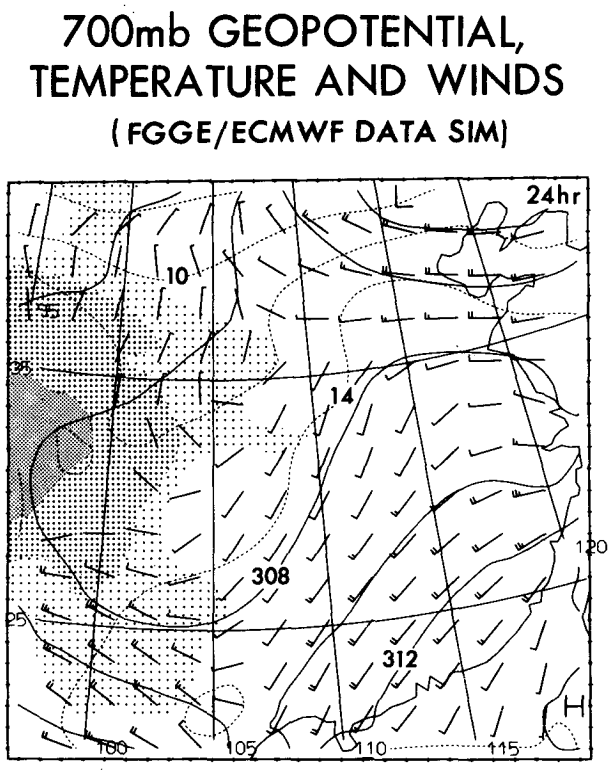

FIG. 6. As in Fig. 4c but taken from a simulation using the original ECMWF/FGGE dataset.

tributions along line segment, *CC'*, indicated in Fig. 7, plotted from ECMWF/FGGE and GFDL/FGGE analysis, respectively. In contrast to the GFDL data analysis, an inversion layer exists between 500 and 1500 m in the ECMWF data analysis. The temperature at sea level is about 30°C from the GFDL/FGGE data but only 22°C from the ECMWF/FGGE data. Other zonal and meridional cross sections display similar features. Comparing with weather map and rawinsonde data, we found that the GFDL analysis is much closer to the observed values below 2 km. For instance, for the selected four points shown by triangles in Fig. 1, the average lapse rate below 1500 m are 5.5, 4.5 and 0°C km^{-1} for GFDL/FGGE, weather map data and EMWF/FGGE, respectively. We also have calculated the monthly mean lapse rate from the surface to 850 mb in July as averaged over five stations: Chendu, Chengqing, Hanzhong, Wuhan and Yichang, the locations of which are indicated by circles in Fig. 1. The resulting mean lapse rates are 5.5 and 4.5°C km^{-1} for 1200 UTC (local time: 7 pm) and 0000 UTC (local time: 7 am), respectively, in close agreement with the GFDL/FGGE analysis. On the other hand, the relative humidity field analyzed by ECMWF/FGGE has a distribution comparable to that analyzed by GFDL/FGGE and to observations.

Based upon our comparison, we conclude that the temperature below 2 km from the ECMWF analysis has a systematic bias and needs to be modified before being interpolated to the present model grid. To eliminate the erroneous temperature inversion we simply reconstruct the boundary layer temperature profile at levels 1.5, 0.5 and −0.5 km according to constant lapse rate of 5.0°C km^{-1}. At the same time, the relative humidity remains unchanged. We shall refer to the model integration with the modified ECMWF/FGGE data as the control simulation.

5. Analysis of the control simulation: The vortex structure

In Fig. 7, simulated tracks of 700- and 500-mb vorticity centers from the control run are compared with the corresponding observed tracks for the 36-hour period from 0000 UTC 14 July through 1200 UTC 15 July 1979. During the 24–36 hour period when the cyclonic vortex had been established, the displacement and the vorticity intensity of the simulated vortex are, in general, quite comparable to observations, although the vortex positions were shifted to the north of the corresponding observed locations. Before the formation of the vortex, at hour 12, the discrepancy at 700 mb is prominent: observations show a positive relative vorticity center over the Sichuan Basin, while the simulation exhibits a positive vorticity center much closer to the edge of the plateau.

At hour 24 (0000 UTC 15 July), the 700-mb wind, temperature and geopotential height fields from the control run (Fig. 9a) indicate a well-defined cyclonic

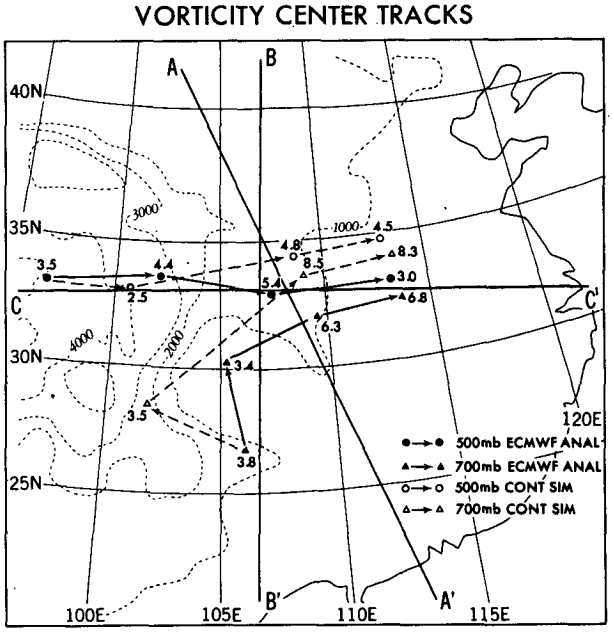

FIG. 7. Comparison of relative vorticity center tracks for every 12 hours from 0000 UTC 14 July through 1200 UTC 15 July. Line segments, *CC'*, *AA'* and *BB'*, indicate positions of vertical cross sections used in Figs. 8, 11 and 12, respectively. The dashed curves are topographic contours in units of meter.

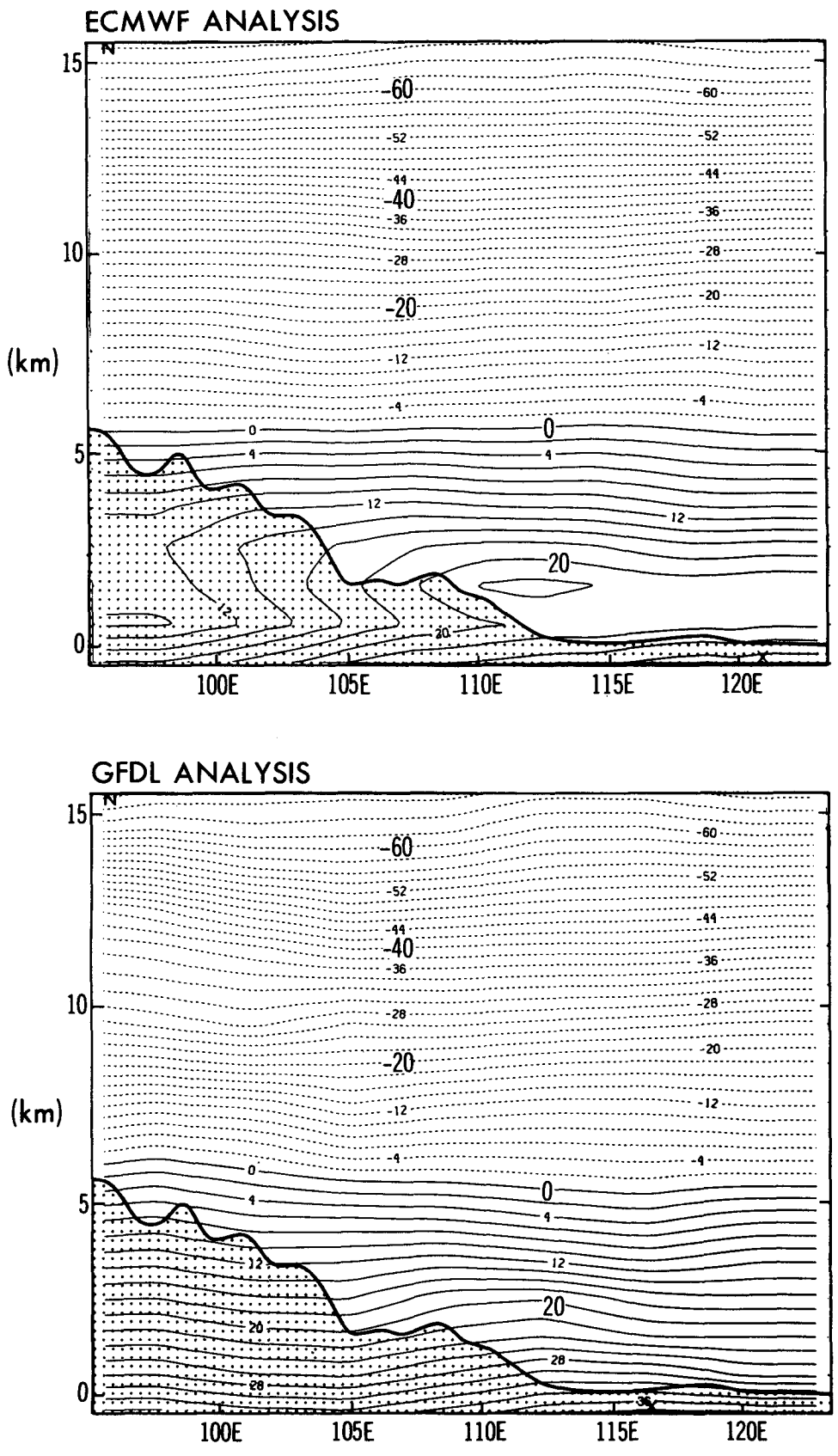

FIG. 8. Comparison of vertical cross sections of temperature (in units of °C) at the initial time (0000 UTC 14 July 1979) along line segment *CC'* shown in Fig. 7.

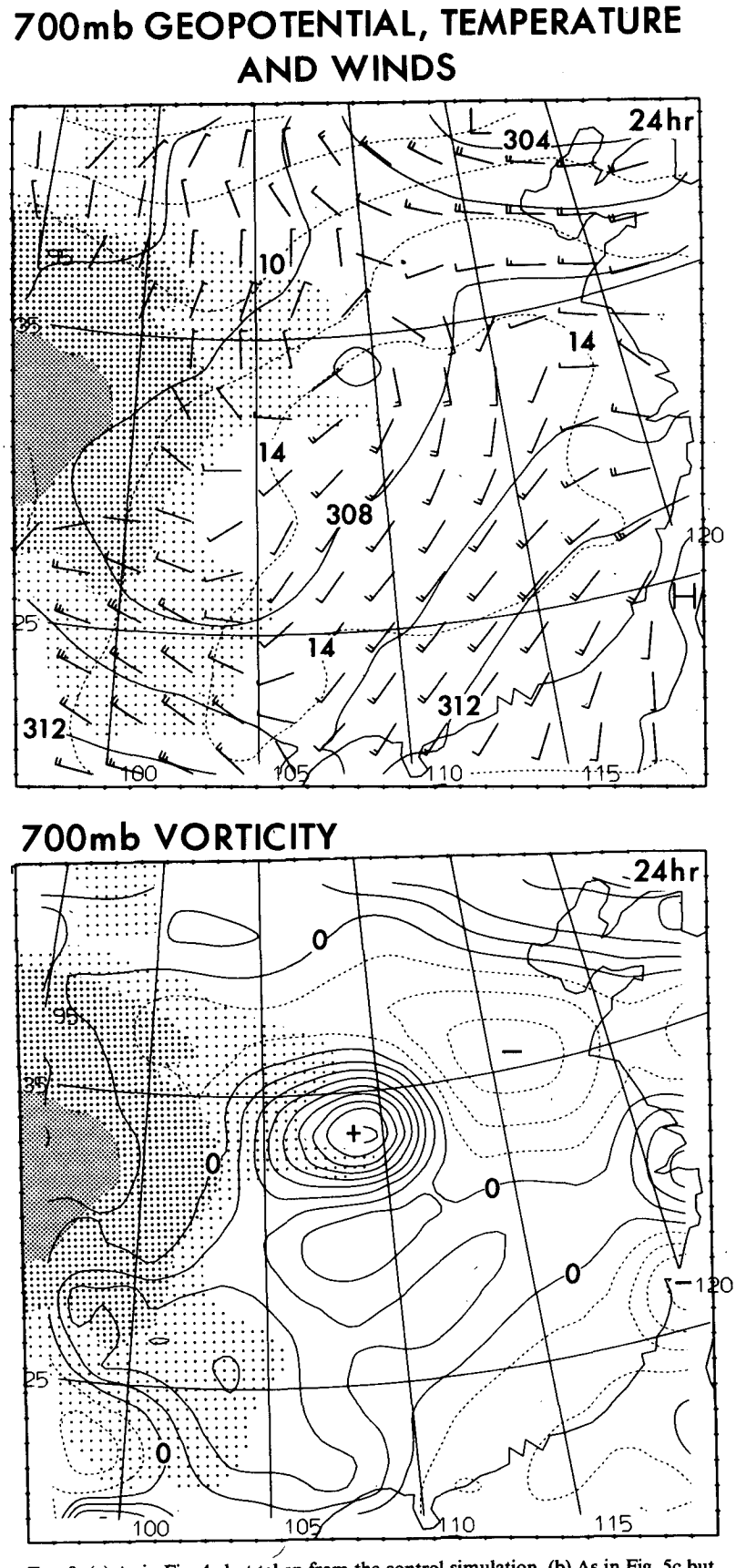

FIG. 9. (a) As in Fig. 4c but taken from the control simulation. (b) As in Fig. 5c but taken from the control simulation.

circulation formed on the lee side of the Tibetan Plateau around (34°N, 109°E). Its horizontal dimension is smaller than that shown by the FGGE data analysis (Fig. 4a), while its maximum vorticity (Fig. 9b) is larger. Taking the vorticity contour of 10^{-5} s^{-1} as a measure of the vortex boundary, one finds the diameter across the vortex center in the east–west direction to be about 800 km for the simulated vortex versus about 1100 km for the observed vortex (Fig. 5a). The stronger vorticity intensity and smaller horizontal scale of the simulated vortex is partially attributed to the difference in spatial resolution of the FGGE analysis and the model simulation. The analyses in the FGGE data are based upon a grid size of 187.5 km, which is twice as large as the present model resolution. Thus, as far as the verification of the model is concerned, it may be more relevant to average the model results over a horizontal area of approximately $4\Delta x^2$, where Δx is the model resolution; this would effectively enlarge the horizontal dimension of the vortex and lessen its maximum intensity at the vortex center. The location of the simulated vortex, as defined by the location of its maximum vorticity, is 200 km north of the observed one. Consequently, in the control simulation (Fig. 9a), the northerly flow behind the vortex did not reach the western Sichuan Basin and failed to combine with the WNW wind that flows around the southeast corner of the plateau (this part of the highland is called Yun-Gui Plateau); hence the positive vorticity region associated with the vortex tends to separate from the positive vorticity region over the Yun-Gui Plateau (Fig. 9b). In contrast, since the observed vortex is located 2 degrees of latitude to the south, its main positive vorticity region tends to connect with the positive vorticity region that is associated with the flow moving over the Yun-Gui Plateau and forms an elongated shape in the southwest–northeast direction. In addition, the leading side (in the direction of motion) of the simulated vortex exhibits a much larger vorticity gradient and a much smaller horizontal extent (Fig. 9b) compared with the observed vortex. In front of the observed vortex, there is an identifiable warm frontlike cyclonic wind shear which is missing in the simulation.

Figure 10a shows contours of the first 24-hour (0000 UTC 14 July–0000 UTC 15 July) accumulation of precipitation in the control simulation (solid curve) versus the observed precipitation (dashed curves). Although the maximum precipitation of 51 mm in the simulation is significantly smaller than the observed maximum (108 mm), the location of the largest rainfall is quite close to observations with an error of less than 100 km. Furthermore, the observed rainfall distribution is obtained by subjective analysis using individual weather station reports without any smoothing and this may, to some extent, account for the difference between the observed and simulated maxima. The primary discrepancy is that the model precipitation is concentrated within a smaller area around the vortex center, whereas the observed precipitation spreads over a larger area elongated in a zonal direction; hence the simulated rainfall area only coincides partially with the central part of the observed rainfall area. The observed excessive rainfall east of the simulated rainfall area is most likely caused by the observed warm frontlike shear line ahead of the vortex, which is missing in the simulation. On the other hand, the observed larger precipitation falling over the region west of the simulated rainfall area results possibly from the fact that the control simulation failed to predict the rainfall in the early stage of development near the plateau boundary and northern Sichuan Basin. As will be shown in section 7, inclusion of the "thermal effect" of the plateau will accelerate the model precipitation process and make the 24-hour precipitation cover a portion of the plateau edge area (Fig. 10c). Lack of latent heat release over the Sichuan Basin in the early stage may be responsible for the model's failure to simulate the 700-mb vorticity center over the Sichuan Basin at hour 12 as mentioned in the beginning of this section.

Figure 11 illustrates a vertical cross section (approximately NNW–SSE, as shown by the line segment AA' in Fig. 7) indicating the wind vector in the plane, the wind component normal to the plane, and relative vorticity and temperature, all at hour 24 for the FGGE analysis (a, b) and the control simulation (c, d), respectively. There are several features common to both analysis and model result, although details may be quantitatively different. They are summarized as follows:

1) The vortex is a shallow system, separate from the westerly jet and the polar front. The observed closed cyclonic circulation extends from the surface (1.5 km) up to 5 km (Fig. 11a); the simulated flow also shows small vertical extent for the closed cyclonic circulation (Fig. 11c). Both of them indicate that the strongest cyclonic circulation appears at about level $k = 4$ (2500 m), corresponding to the top of the planetary boundary layer following the topography. The vortex developed beneath a strong upper tropospheric anticyclonic vorticity region (Figs. 11b, d). Notice also that an anticyclonic vorticity region separates the vortex region from the positive vorticity region associated with the upper tropospheric westerly jet and polar front. The suggestion here is that the development of the shallow low-level warm vortex is dynamically independent of the westerly jet.

2) The strong WSW wind component south of the vortex center (Fig. 11a) indicates the existence of a prevailing southwest low-level jet at 1.5 km. On the other hand, the simulated ENE wind north of the vortex center is much weaker, by a factor of 2. The acceleration of the low-level SW jet located between the vortex and the WPSH is closely related to the intensification of the vortex itself in both the simulation and the FGGE analysis. The low-level SW jet in the control solution

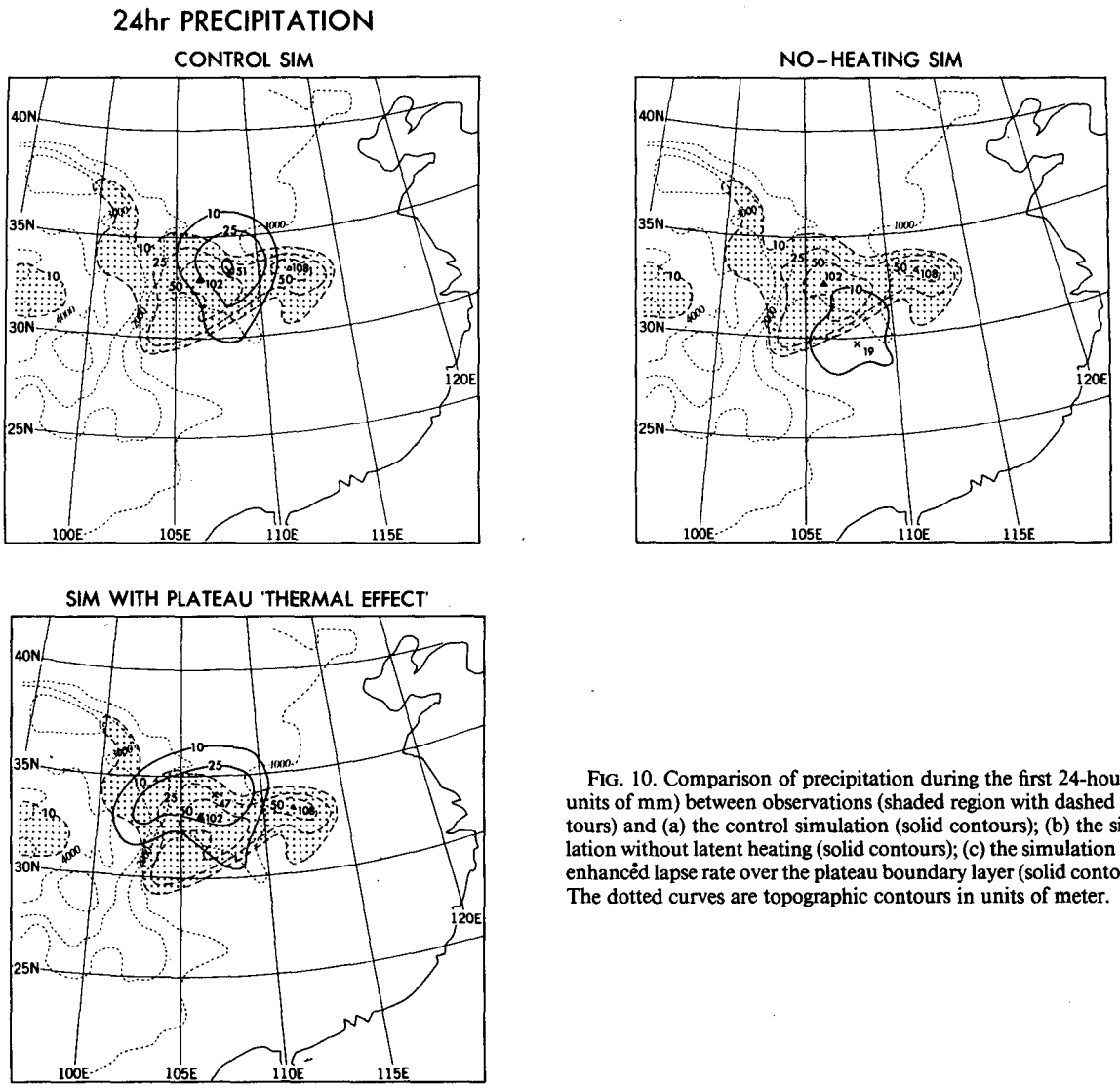

FIG. 10. Comparison of precipitation during the first 24-hour (in units of mm) between observations (shaded region with dashed contours) and (a) the control simulation (solid contours); (b) the simulation without latent heating (solid contours); (c) the simulation with enhanced lapse rate over the plateau boundary layer (solid contours). The dotted curves are topographic contours in units of meter.

has a maximum speed of only 13 m s^{-1}, which is considerably weaker than that analyzed from FGGE data, which is 24 m s^{-1}. This discrepancy occurs because the simulated pressure gradient between the vortex and WPSH is weaker due to: (i) the northward shift in the vortex location, (ii) the higher minimum pressure at the vortex center, and (iii) the weaker strength of the WPSH in the simulation. In the upper troposphere, a strong westerly jet is located at 12 km height, about 700 km north of the 700-mb vortex center, whereas a subtropical easterly jet is found to be located at 15 km height and about 1100 km south of the 700-mb vortex center (Fig. 11a, c).

3) Intense upward motion is concentrated within a region near the 700-mb vortex center with a maximum of the order of 10 cm s^{-1}. The ascending motion in the FGGE analysis extends from the surface up to the tropopause, and the simulated ascent extends up to 12000 m but with a stronger intensity. There is a pronounced northward transport of mass and moisture toward the vortex center near the terrain surface (Fig. 11a, c). In sharp contrast, the southward cold advection toward the vortex center is hardly significant. In this cross section, the upper-level divergent flow is significantly weaker in comparison with the surface-layer convergent flow and mainly southward.

4) Warm air occurs south of the vortex center, while a weak, narrow "cold wedge" covers a part of the northwest side of the vortex (Fig. 4b and Fig. 9a). As a result, a weak temperature gradient developed by hour 24. In the vertical cross sections (Fig. 11b, d), the constant temperature contours tilt downward to the north only at the north portion of the vortex. Note that this weak baroclinicity is a consequence of the development of the vortex. The asymmetric thermal structure (warm in the south and center, cool in the north)

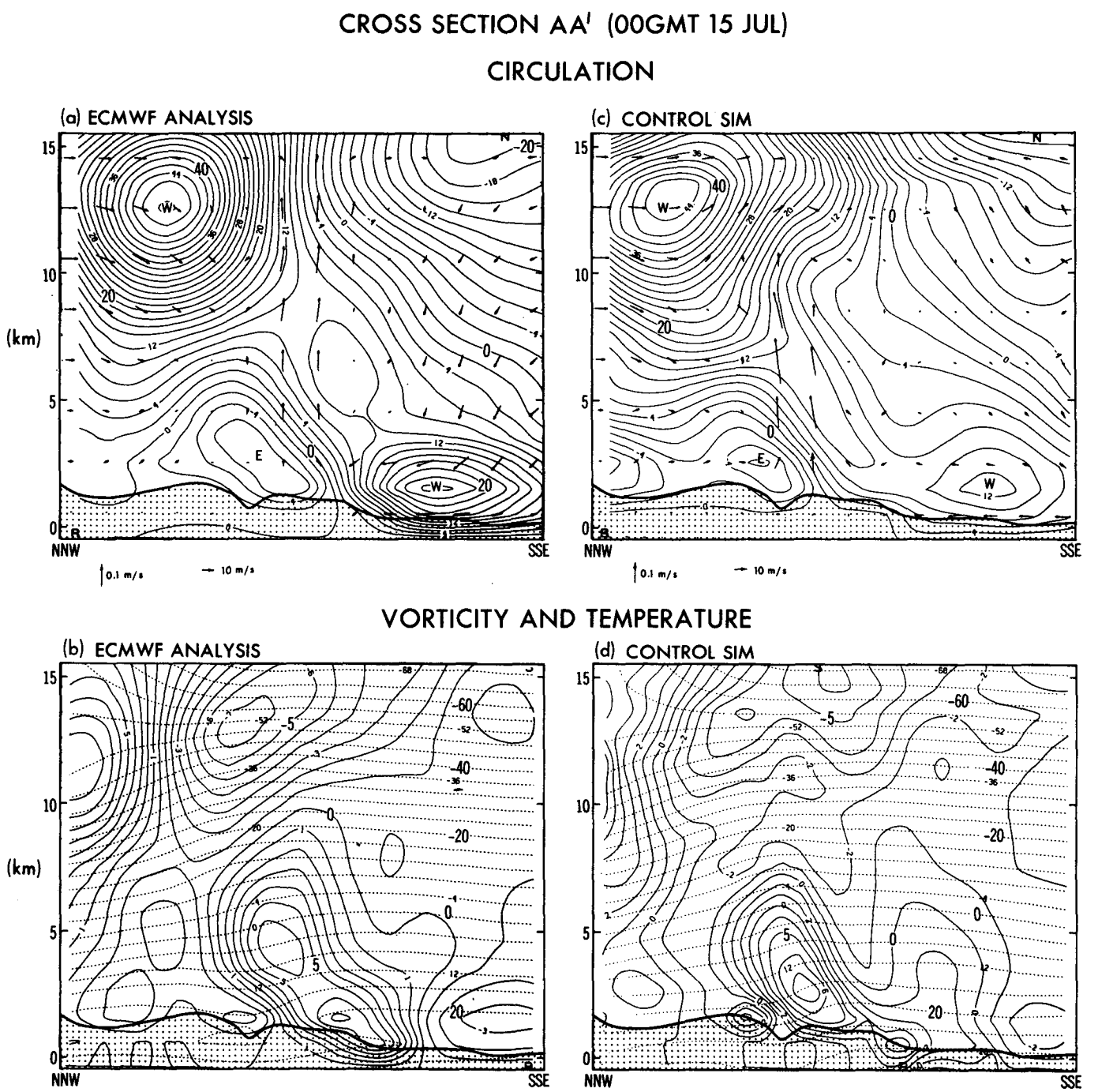

FIG. 11. Maps of observed vertical cross section, *AA'*, indicated in Fig. 7, showing (a) winds in the plane (vectors), and wind speed normal to the plane (contours, in units of m s^{-1}); (b) vorticity (solid contours, in units of 10^{-5} s^{-1}) and temperature (dotted contours, in units of °C). Figures 11(c) and (d) are the same fields as in Fig. 11(a) and (b), respectively, but taken from the control simulation. The shading represents the plateau terrain.

would disappear if the amount of the rainfall were reduced, as was the case in the simulation with unmodified FGGE data (not shown), suggesting that the existence of this temperature contrast is linked to the precipitation and warm advection. The extent of the cold wedge is somewhat underestimated by the simulation. This may be due to the exclusion of the evaporation of falling rainwater in the present simulation.

In accordance with the thermal structure, the vortex axis shown by the zero line of the WSW wind speed in Fig. 11a, c tilts northward with height up to 5 km where the closed cyclonic circulation disappears. The

vorticity maximum coincides with vortex axis below 5 km and tends to tilt southward with height above 5 km in the observation but is upright in the simulation.

Using the same corrected initial dataset as used in the control simulation, we have performed other experiments for various model parameters. The results indicate that all the simulations have similar defects in their predictions, namely, a northward shift of the vortex position at hour 24 and a lack of latent heat release and vorticity generation over northern Sichuan during the first 12 hours. It is speculated that these systematic errors may have been introduced by changes we have made for the FGGE IIIb data (section 4). When we modified the temperature profiles at levels of 1500 and 500 m, we assumed a constant lapse rate everywhere (5°C km^{-1}) while leaving relative humidity unchanged. In this way, the horizontal distribution of mixing ratio and the conditionally unstable stratification have been changed accordingly. The latter would affect, to some extent, the distribution and strength of the latent heat release which is involved in the vortex development. We have compared the observed sounding at Chengdu (see Fig. 1) with that derived from the corrected FGGE data at gridpoint (10, 14) in the model for the initial time. It was found that the level of free convection occurs at 850 mb for the observed sounding and 650 mb for the model sounding. Similar results are obtained when we compare the station sounding at Yibin (see Fig. 1) with the model counterpart at grid point (10, 12). The difference between the observed and model unstable stratification over the Sichuan Basin may explain why the model simulation produced much less precipitation in the northern Sichuan Basin if we assume that the dynamic forcing is comparable in the both cases during the first 12 hours. Both lack of initial vorticity development over the north Sichuan and the northward shift of the 24-hour vortex center are quite possibly accounted for by this factor.

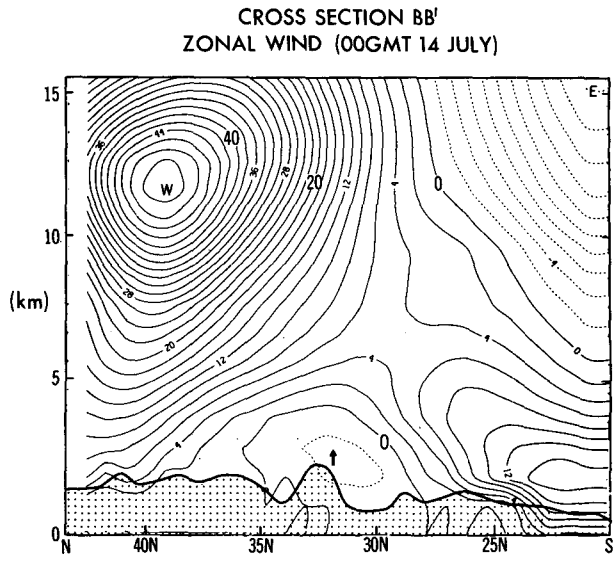

FIG. 12. Plot of vertical cross section, *BB'*, indicated in Fig. 7, showing zonal wind (contours in units of m s^{-1}) at 0000 UTC 14 July 1979. The shading shows the plateau terrain; arrows indicate locations of the vortex that formed 24 hours later.

6. Mechanism for vortex development

In this section we shall analyze the temporal evolution of the simulation with emphasis on identifying the mechanisms that may be responsible for the vortex development. We shall begin our analysis by showing that the vortex was formed in a region where the dynamic energy of the mean flow available for vortex development was rather limited.

a. The analysis of possible baroclinic and barotropic energy sources

Some of the possible eddy energy sources lie in the vertical and horizontal shear of the environmental flow in which the disturbance is embedded. Figure 12 shows a vertical cross section of the zonal flow along the 106.5°E longitude 24 hours prior to the formation of the heavy rain vortex (0000 UTC 14 July 1979). The most impressive feature is the presence of an archlike, nearly stagnant region, located between 27° and 37°N near the terrain surface. This is apparently a consequence of the blocking effect of the Tibetan Plateau. The vortex that was most intense around 3 km formed 24 hours later in this low-wind region, where both vertical and horizontal shears almost vanish. It is clear that the local energy source in the mean flow is not available to any disturbance, pointing to the importance of an alternative diabatic energy source in the vortex formation region. In the neighborhood of the stagnation region, areas exist in which the environmental flow satisfies necessary conditions for dynamic instability. First, the region south of 25°N below 4 km shows a wind maximum of 14 m s^{-1}. This corresponds to the low-level southwest jet which runs from the south of the plateau (northern India and the Bay of Bengal) along the northwest edge of the WPSH (Fig. 4a). The horizontal shear lying between the stagnation region and the WSW jet (around 26°N on the cross section along 106°E) makes the meridional gradient of the absolute vorticity, $\beta - \partial U^2/\partial y^2$, vanish, thereby satisfying the necessary condition for barotropic instability (note that we have neglected the vanishingly small vertical shear and treat the WSW flow as a zonal westerly flow). In addition, over the northern part of the stagnation region below 7 km, vertical shear varies sharply from nearly zero within, to a finite value outside, the stagnation region. Since horizontal shear is weak there, the abrupt increase in the vertical shear across the top of the stagnation region also makes the meridional gradient of the environmental potential vorticity

$$\beta - (f_0^2/N^2\rho_s)/(\partial\rho_s/\partial z)(\partial U/\partial z) - (f_0^2/N^2)(\partial U^2/\partial z^2)$$

vanish, so that internal baroclinic instability may be possible. It is not clear, under what conditions or to what extent, these local energy sources could be available to produce significant disturbances. Due to the existence of the elevated steep topography and complicated three-dimensional nature of the mean flow, the analysis of dynamic instability of the initial basic state over the eastern flank of the plateau is extremely difficult. We shall investigate this problem by means of comparative numerical experiments in which particular processes are purposely eliminated.

b. Roles of convective latent heating in the vortex development

A "nonlatent heating" simulation has been performed, for which all the model parameters are exactly the same as those used in the control run except that the latent heating is excluded from the model thermodynamic equation. The simulation at 700 mb for wind, temperature and geopotential height fields at hour 24 are presented in Fig. 13. Outside the lee side low-wind region, which is roughly confined between 27° and 37°N and between 102° and 112°E, the flow fields are remarkably similar to those simulated in the control run (Fig. 9a). However, the vortex that formed in the stagnation region in the control run is now totally missing. In fact, it never developed during the entire

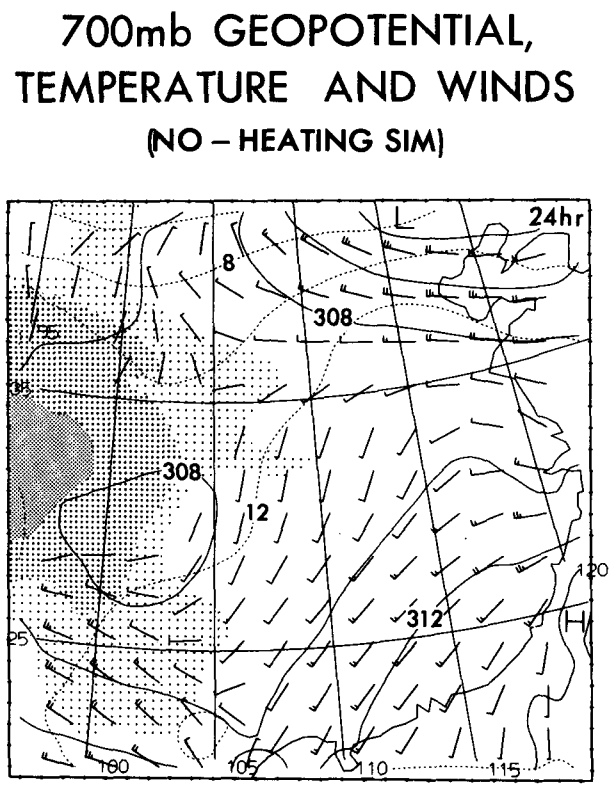

FIG. 13. As in Fig. 4c but taken from the simulation without latent heat.

period of the 36-hour integration. The corresponding temperature field in the stagnation region decreases by about 2°C on average; thus, the temperature contrast that appears in the northwest part of the stagnation region in the control run now becomes weak. We note that the precipitation accompanying the vortex formation results in a local warming in the control solution, implying that the latent heating is primarily released by cumulus convection rather than by stable precipitation. The reason for this is that stable precipitation always tends to be accompanied by a cold core due to the fact that the local moist adiabatic lapse rate is steeper than the lapse rate in a stable saturated environment. The comparison between the control and the nonlatent heating experiments demonstrates the dominant role that convective latent heating plays in the generation and development of the heavy rain vortex, as well as in the enhancement of the temperature contrast on the northwestern side of the developing vortex. It also suggests that, without convective latent heating, the dynamic instability of the environmental flow alone is unable to initiate the observed disturbance. This result contrasts with results presented in other studies, which suggest that the warm southwest vortex is generated without regard to whether latent heating is included or not (e.g., Hovermale, 1983), i.e., vortex-genesis results from the dynamic instability of the large-scale flow interacting with the elevated plateau topography, while latent heating merely enhances its later intensification. For the case studied here, the dynamic (barotropic, baroclinic or topographic) instabilities are shown to be too weak to generate a vortex.

From the distribution of 24-hour accumulated precipitation shown in Fig. 10b for the nonlatent heating solution, it is seen that, without latent heating, rainfall of only 19 mm occurs over the southeast stagnation region. The corresponding horizontal distribution of the vertical motion at hour 12 is shown in Fig. 14b. In the absence of latent heating, the dynamic forcing that initiates precipitation is located on the southeastern edge of the stagnation region, where the strong horizontal shear associated with the WSW flow is present. On the other hand, with the latent heating included, the 24-hour precipitation increases dramatically with a maximum rainfall of 51 mm near the vortex center or in the central stagnation region (Fig. 10a). The corresponding upward motion at hour 12 also shifted to the central stagnation region (Fig. 14a) with a maximum ascent of 5.6 cm s^{-1}, which is 2.7 times as large as that in the nonlatent heating case. The center of this intense ascent is caused by both the differential vorticity advection and the latent heating, as will be described in the next subsection.

c. The triggering and intensification of the vortex

We now focus our attention on initiating mechanisms for the vigorous cumulus convection and low-level vortex intensification. At the initial time a no-

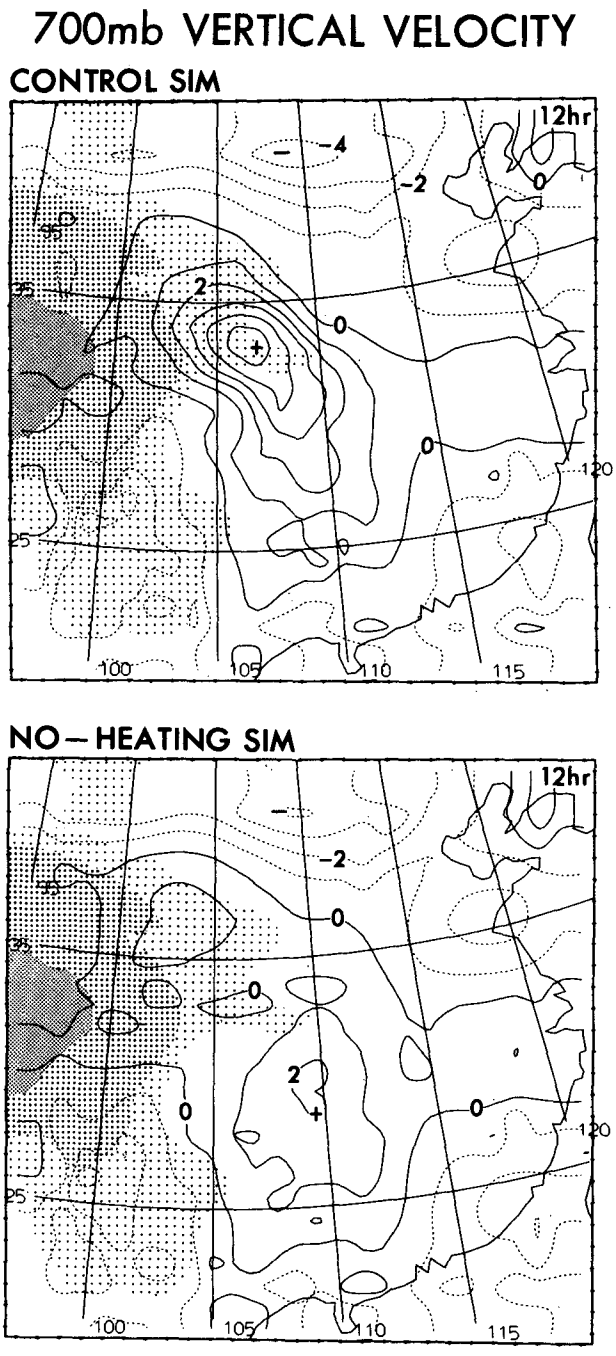

FIG. 14. Plots of 700-mb vertical velocity in units of cm s^{-1} at 1200 UTC 14 July taken from (a) the control simulation and (b) the simulation without latent heat. Shading as in Fig. 4.

ticeable shallow mesoscale low disturbance and associated trough had been present in the plateau boundary layer (Fig. 3); the location of the vorticity center is indicated in Fig. 7. Figures 15 and 16 display the vertical cross sections of vertical and zonal velocity, relative vorticity and cloud water content along the approximate latitude 33°N for the nonlatent heating (6–24 hour) and control (12–36 hour) runs, respectively. In the absence of the latent heating, the positive vorticity associated with the initial plateau disturbance was weakening continuously as it slowly moved downstream; by the time it reached the plateau boundary (103°E), the ascending motion in front of it became too weak to trigger vigorous convective activity (Fig. 15b). In sharp contrast, for the control run, the feedback of the latent heating maintained the strength of the initial triggering disturbance and enhanced the upward motion as it moved eastward. By hour 12 (Fig. 16a), a strong ascent region in advance of the triggering disturbance was positioned over the western part of the stagnation region. The vertical motion and convergence within the stagnation region is partially induced by the differential vorticity advection between the middle troposphere and the surface: strong positive vorticity at the 500-mb level versus zero advection near the surface in the stagnation region. In order to compensate for the divergence induced by latent heating in the upper troposphere, low-level convergence within the stagnation region is also required. It is clear that the dynamic forcing due to mass compensation for the latent heating-induced upper level divergence and due to differential vorticity advection is primarily responsible for the triggering of the vigorous convection in the lee-side stagnation region. It is important to notice that the strength of the triggering is determined by the latent heating over the main body of the plateau. In this sense, the observed precipitation spreading over the eastern plateau (Fig. 2b) may be a relevant indicator of the initiation of the SW vortex.

The process of the onset of vigorous convection and spinup of the vortex in the control simulation can be clearly observed from Fig. 16. During the first 12 hours, the plateau disturbance moved eastward very slowly at a speed of about 100 km per 6 hours, and the corresponding vorticity center occurs at 5500 m (Fig. 16c). When a region of significant ascending motion was positioned over the western stagnation region at hour 12, rapid expansion of the model "convective" cloud took place during the next 6 hours (Fig. 16a, b): the vertical extent of the cloud layer increased by 3–4 km, and the location of the maximum of cloud water jumped from 6500 m to 8500 m; meanwhile the vorticity center suddenly moved down to 2500 m and to a position 700 km east of the previous location. These abrupt changes indicate the onset of vigorous convection over the lee side. During this 6-hour period, the maximum upward velocity was enhanced by a factor of 2 to 3, and the horizontal phase difference between the upward motion and positive vorticity fields decreased from 90° to nearly zero. One should notice, however, that the maximum vorticity of the vortex is almost unchanged during this period. Dramatic intensification in the vorticity field occurred after the onset of the vigorous convection from hour 18 to hour 24 (Fig. 16b, c): the maximum vorticity increased sharply

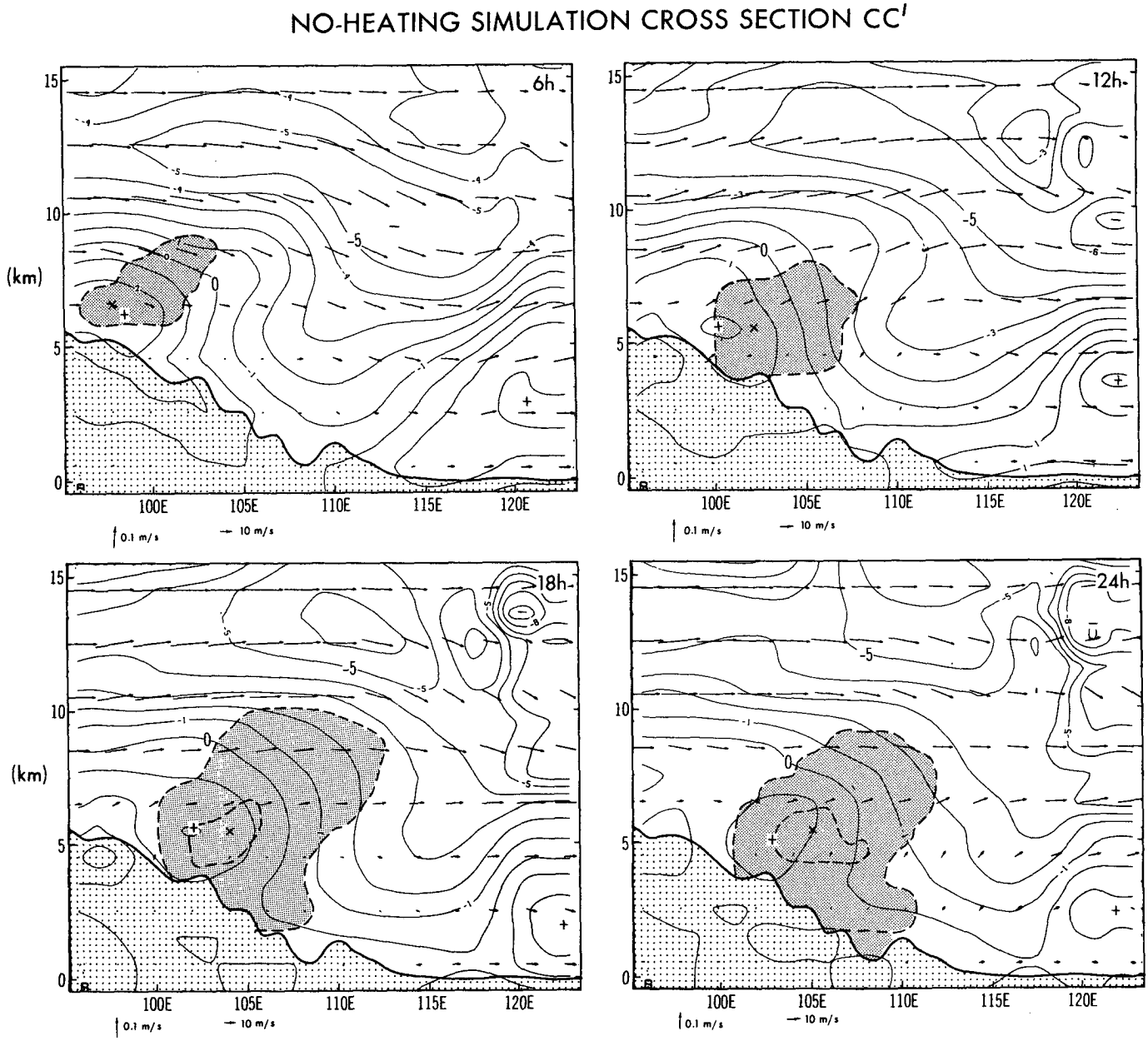

FIG. 15. Plots of vertical cross section of vorticity (solid contours in units of 10^{-5} s^{-1}), wind in the plane (vector), and cloud water (dense shading with dashed contours in units of 0.4 g m^{-3}) in nonlatent heating solution for (a) 0600 UTC; (b) 1200 UTC; (c) 1800 UTC 14 July; and (d) 0000 UTC 15 July. The cross section is taken along the east–west direction and through 700-mb vortex center at hour 24. The shading below the thick solid curve indicates the area beneath the terrain surface.

from 3 to 8.1 ($\times 10^{-5}$ s^{-1}). The fact that the establishment of a strong upward motion leads to the spin-up of the vortex suggests the following development process. The bulk effect of convective heating first generates a mesoscale, direct secondary circulation characterized by an upper-level divergence and a low level convergence. In the presence of sufficient strong planetary vorticity, the low-level convergence generates a cyclonic tendency, thus causing the vortex to spin up. A linear analysis of a CISK (Conditional Instability of the Second Kind) model has demonstrated that the preferred unstable wavelength is proportional to the inverse of the Coriolis parameter (Wang, 1987a). The typical scale for the most unstable CISK disturbance at 33°N should be half of that which would occur at 15°N. The latitude factor, along with the scale of the plateau triggering disturbance, is important in setting up a smaller characteristic horizontal dimension for the SW vortex.

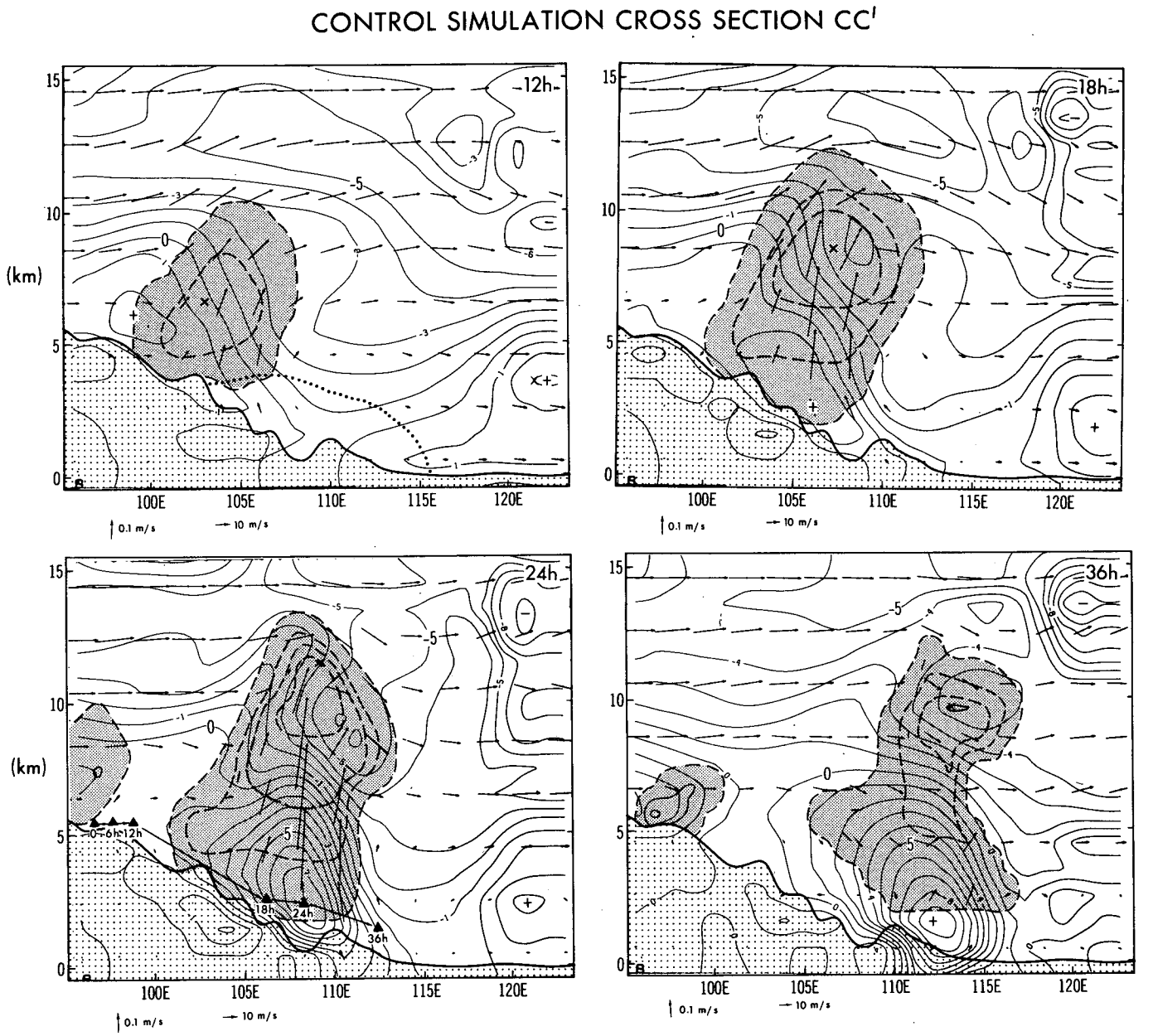

FIG. 16. Plots of vertical cross section of vorticity (solid contours in units of 10^{-5} s^{-1}), wind in the plane (vector), and cloud water (dense shading with dashed contours in units of 0.4 g m^{-3}) in the control solution for (a) 1200 UTC, (b) 1800 UTC 14 July, (c) 0000 UTC, and (d) 1200 UTC 15 July. The cross section is taken along the east–west direction and through the 700-mb vortex center at hour 24. The triangles in Fig. 16c indicate the locations of the vorticity center with time beneath. The shading beneath the thick solid curve shows the area below the terrain surface. The region between the dotted curve and the terrain surface in Fig. 15a is the stagnation region where wind speed is not greater than 2 m s^{-1}.

7. The thermal and dynamical forcing of the Tibetan Plateau

Topography generally has a fundamental influence on the atmospheric flow over and/or around it. The influence of mechanical forcing on the formation of a mesoscale vortex that occurred on the lee side of the Tibetan Plateau was numerically studied by Wu and Chen (1985). Due to the crude model resolution, their results probably mainly show the influence of the mechanical forcing of the plateau on the large-scale background flow, which affects indirectly the formation of the mesoscale vortex. Here we shall concentrate on a discussion of the influence of the plateau on the warm SW vortex formation in the framework of a limited-area mesoscale model. Both thermal and dynamic processes are involved.

Since the disturbances over the plateau could serve as initial triggering mechanisms for the SW vortices when they move off the plateau, the thermal influence

of the plateau is expected to have an impact on initiation of the SW vortex by changing these triggering disturbances. The plateau environment in summer is favorable for generating thermally driven disturbances, mainly due to the following reasons (Wang, 1987b): 1) latent heat is released in a shallow layer located in the upper troposphere where the heat capacity of the air column per unit of surface area is substantially smaller; 2) the static stability parameter over the plateau is dramatically reduced; and 3) the moisture content in its boundary layer is considerably higher than in the surrounding air. Reasons 2 and 3 are results of the sensible and latent heat fluxes from the elevated surface. In the present model, since the sensible heat flux is proportional to the temperature gradient at the surface, a change in the lapse rate at the surface implies a change in the sensible heat flux. To examine the response of the model atmosphere to the increase of the sensible and latent heat fluxes at the plateau surface, we assume that, at the initial time, the lapse rate in the boundary layer (from the terrain surface to 1 km above the surface) over the plateau (defined by the region where surface is higher than 2 km above sea level) is 6.0°C km^{-1} with the relative humidity unchanged. This lapse rate is slightly greater than the values of the ECMWF/FGGE analysis for most of the plateau boundary layer region. A simulation with this modified initial condition was carried out. The resulting solution is very similar to the control simulation at hours 24 and 36, but appreciable differences exist in the solutions at hour 12. The first 12-hour precipitation shows a maximum of 17 mm located at (33°N, 103°E), in contrast to the corresponding maximum of 6 mm located at (30°N, 108°E) in the control run. The position of the 24-hour precipitation shown in Fig. 10c is apparently in better agreement with the observed rainfall distribution, especially in the region west of 105°E. The 700-mb vorticity fields at hour 12 (Fig. 17a, b) indicate that, with enhanced lapse rate over the plateau, one of the deficiencies of the control solution, i.e., the lack of vorticity development at hour 12, has been improved: a separated weak vorticity center appears around 33°N, 104°E (compare Fig. 17 with Fig. 5a). It is thus suggested that the surface sensible and latent heat fluxes of the elevated plateau may enhance the triggering disturbance and thus may significantly affect the initiation of the warm vortex in its early stage.

We now consider the dynamic effects of the plateau. The observed monthly mean wind at 850 and 700 mb in July shows that southerly flow dominates conditions on the lee side. This low-level northward flow tends to be decoupled from the westerly flow in the middle troposphere flowing over the plateau (e.g., see Yeh and Gao, 1979). Figure 18 displays a vertical cross section of both zonal and meridional velocity along 32°N at the initial time of the model run. Between 102° and 110°E the wind is vanishingly small, while east of 110°E, both components increase rapidly with longitude. The extent of the low-wind region depends upon the interaction between the large-scale circulation and the influences of the entire Tibetan Plateau. Because of the limited size of our domain, a diagnosis of this interaction is beyond the scope of this study. However, from the mesoscale point of view, the presence of the

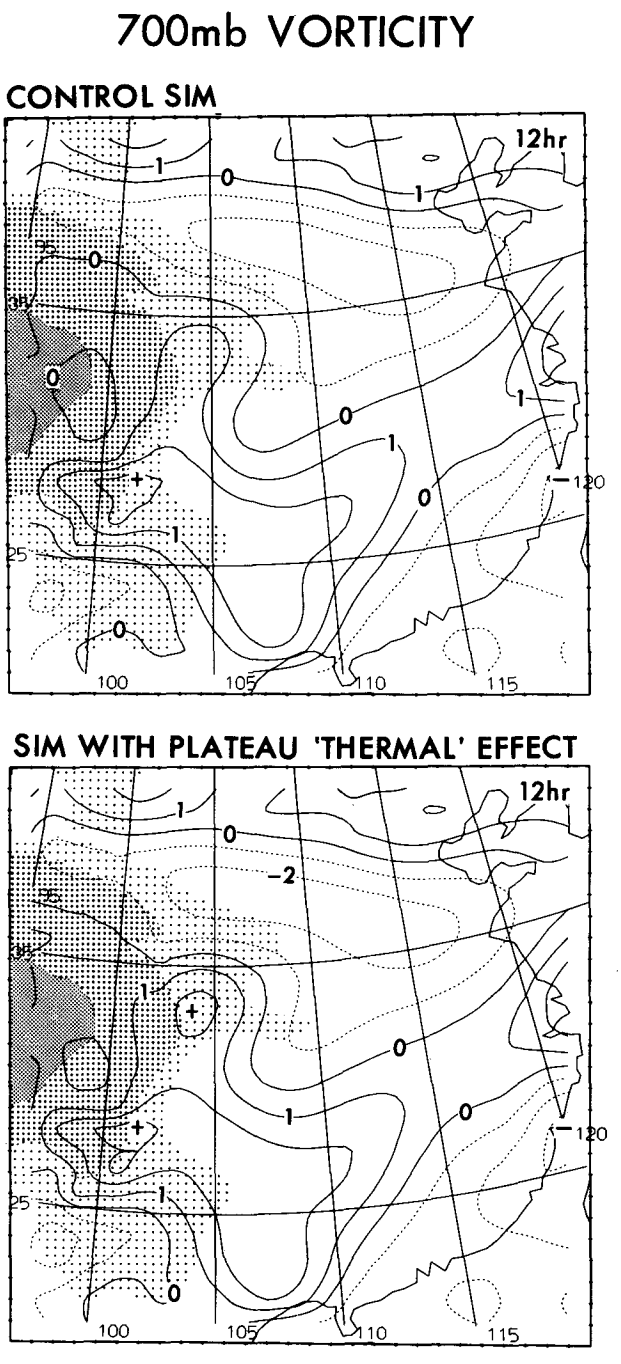

FIG. 17. Plots of 700-mb vorticity (contour in units of 10^{-5} s^{-1}) at hour 12 (1200 UTC 14 July 1979) from (a) the control simulation and (b) the simulation with enhanced lapse rate over the plateau boundary layer. Shading as in Fig. 4.

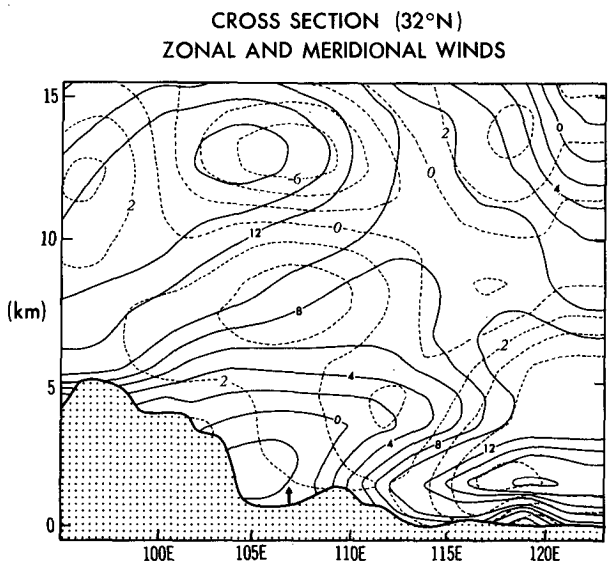

FIG. 18. Plot of vertical cross section along 32°N latitude, showing zonal (solid) and meridional (dashed) wind components (contours in unit of m s^{-1}) at the initial time. The arrows indicate the location of the vortex formation at hour 18. The shading beneath the thick solid curve denotes topography.

stagnation region appears to stabilize the dynamic instability of the large-scale flow to mesoscale disturbances in the following way. First, it diminishes vortex stretching usually found in the lee side as the flow moves down slope. It also prevents horizontal convergence on the lee side due to the low-level convergent flow moving around the plateau. Finally, the presence of the stagnation region may effectively eliminate the potentially destabilizing effect of the topographic slope to baroclinic flows parallel to the height contours, a mechanism that has been discussed by Orlanski (1969). These stabilizing effects of the stagnation region may be relevant in explaining why dynamic forcing alone in the nonlatent heating run is not sufficient to generate the SW vortex.

On the other hand, the plateau blocking provides a favorable environment for the development of cumulus convection and associated rotational disturbance once convection is organized by certain initial mesoscale forcing. The extremely steep south slope of the plateau often deflects the low-level southwest Indian monsoon, forcing it to move along the topographic contours toward the lee side. In particular, when the WPSH extends abnormally westward, the enhanced, deflected low-level southerly flow transports abundant vapor to the eastern flank of the plateau. As a consequence, a high mixing ratio region extends from the south to the east Sichuan Basin (not shown). The accumulation of moist static energy in the lower layers increases convective instability.

We have designed an experiment in which realistic topography is replaced by a modified cylindrical plateau in order to confirm the dominant blocking effect of the plateau. This was done by keeping the surface height above 3000 m unchanged and reducing the remaining surface heights that are between 500 and 3000 m to a height of 500 m. The rest of the parameters are the same as those used in the control run. The purpose of this experiment was to isolate the blocking effect and to examine the response of the model to the removal of the plateau slope. It was found that the solutions at hours 18 through 36 basically resemble the corresponding control solutions, although the vortex position shifts to northeast by about 100–200 km and the vortex is slightly more intense (e.g., see the simulation after 24 hours shown in Fig. 19a). The result here suggests that, regardless of the change in the topographic configuration, as long as the plateau blocking and latent heating are present, the vortex still forms on the lee side. On the other hand, the control solution and the solution with a "cylinder" plateau are quite different in the first 12 hours. The control solution at hour 6 shows a very weak ascending region with a maximum of only 2–3 cm s^{-1} at the 850- and 700-mb levels. It was only dramatically increased at hour 12 when the plateau disturbance moved to the edge of the plateau. As a result, the vortex formed around hour 18 in the middle of the stagnation region. However, the simulation with a "cylinder" plateau at hour 6 already features a strong upward motion with a maximum velocity of 7.2 cm s^{-1}. As a result, a well-established cyclonic vortex formed at 850 mb around hour 12 with vorticity reaching 7.6×10^{-5} s^{-1} (Fig. 19b). The position where it formed was about 300 km south of the initial vortex position in the control run (Fig. 20). These differences in the early stage reveal different triggering mechanisms in the two experiments. In the "cylinder" plateau case, the absence of the plateau slope eliminates its resistance to the confluent flow moving around the southern and northern edges, so that the convergence due to the confluence produces a strong dynamic forcing on the lee side, which directly triggers the onset of cumulus convection and vortex-genesis. On the other hand, the 500-mb vorticity disturbance moved eastward and attenuated during the first 18 hours (Fig. 20), and thus did not make a significant contribution to the initial development of the simulated vortex. We, therefore, speculate that, under certain favorable circulation conditions, the low-level confluent flow components moving around the plateau periphery could directly contribute to the vortex-genesis on the lee side.

8. Concluding remarks

The lower tropospheric vortices that form over the downwind side of the Tibetan Plateau, or SW vortices, are important disturbances in the general circulation of East Asia. Their intensity and frequency of occurrence have major implications for the flood and drought problems over the middle and lower Yangzi

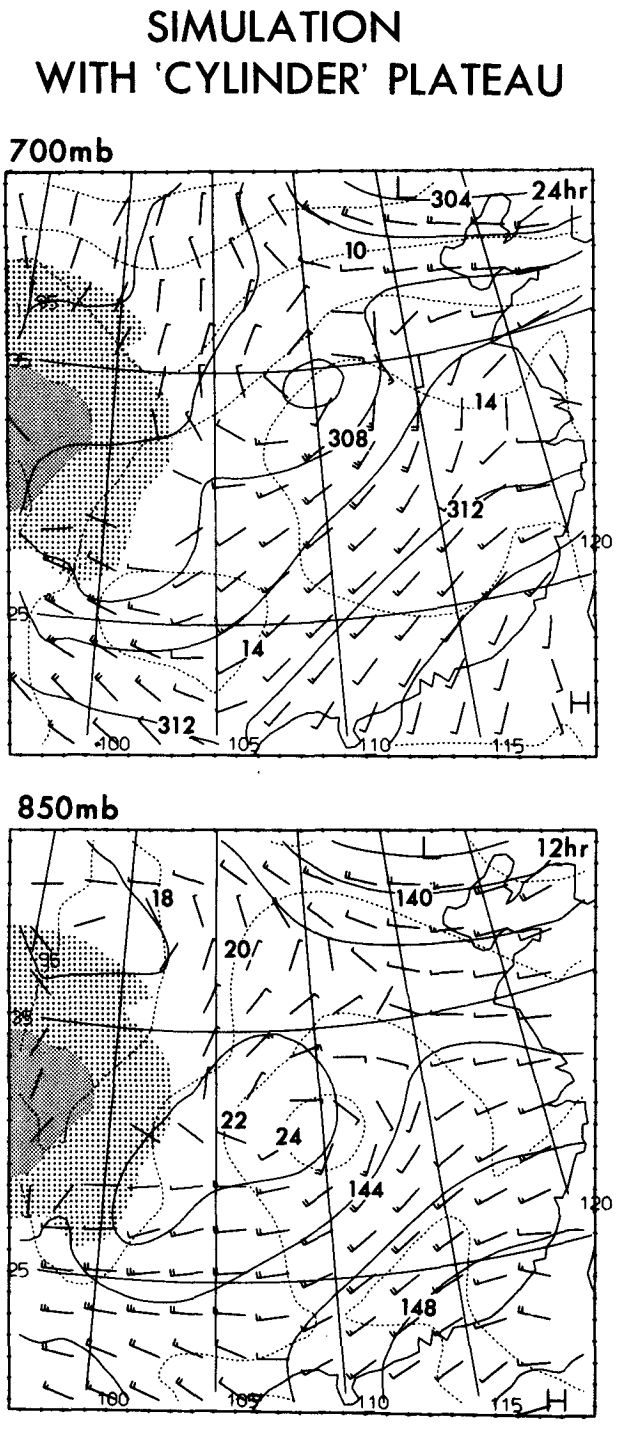

FIG. 19. Plots of geopotential height (in units of 10 m), temperature (in units of °C) and wind fields taken from the simulation with a "cylinder" plateau for (a) 700 mb at 0000 UTC 15 July and (b) 850 mb at 1200 UTC 14 July 1979. The dark and light shadings represent the regions where terrain height are higher than 4500 m and between 3000 m and 4500 m, respectively.

River Valley. Their development, involving interactions between the large-scale flow and the influences of the Tibetan Plateau and between cumulus convection and subsynoptic disturbance, exhibits unique dynamic complexity and variety.

To diagnose the dynamical structure and the development mechanism, an example of the heavy rain SW vortex which occurred during the period of 14–15 July 1979 is investigated using a limited-area mesoscale numerical model. The model includes a parameterization of the effects of the high-resolution plateau topography and an explicit latent heating representation. Using a carefully modified ECMWF/FGGE dataset as initial and boundary conditions, we performed a 36-hour model integration and obtained a reasonable simulation of this case.

The simulated vortex shares many common features with observations in its dynamic structure. These features are discussed in detail in section 5. Some noticeable characteristics are outlined as follows: 1) The developing and mature shallow SW vortex is clearly detached from the major baroclinic frontal zone. 2) Intense upward motion is concentrated near and to the east of the 700-mb vortex center. 3) A 180° phase shift exists between the upper and lower vorticity (and geopotential height) fields. 4) A pronounced northward transport of warm air and water vapor toward the vortex center prevails in the surface boundary layer, while southward advection of cold air toward the center is hardly significant. 5) Warm air extends from the south to the central vortex, whereas a weak cold wedge covers only the northwest portion of the vortex. The formation of the temperature contrast is a consequence of the vortex development.

Since the development of these vortices involves complicated interaction between the background large-scale circulation and the dynamic and thermal effects of the Tibetan Plateau, the authors do not believe that there is a universal mechanism that is responsible for the formation of all SW vortices. The case studied here belongs to one group of the SW vortex (the warm SW vortices). Even for the warm SW vortices, the major triggering mechanism may differ from case to case. In this regard, we tried to test the following hypotheses:

(A) Superposition of a weak middle tropospheric plateau disturbance moving off the plateau on a low-level, moist, conditionally unstable air mass causes the low-level vortex development via latent heat release.

(B) Decoupling from the middle and upper tropospheric flow, the two branches of low-level flow moving around the plateau periphery converge on the lee side and generate positive vorticity. The lateral friction of the steep eastern slope of the plateau may also contribute to the cyclonic vorticity genesis.

(C) The stretching effect for the flow moving downslope on the lee side of the plateau induces cyclonic vorticity genesis.

(D) A low-level northward moist flow with horizontal and vertical shear is destabilized by the slope of the eastern plateau periphery. The mechanism may be

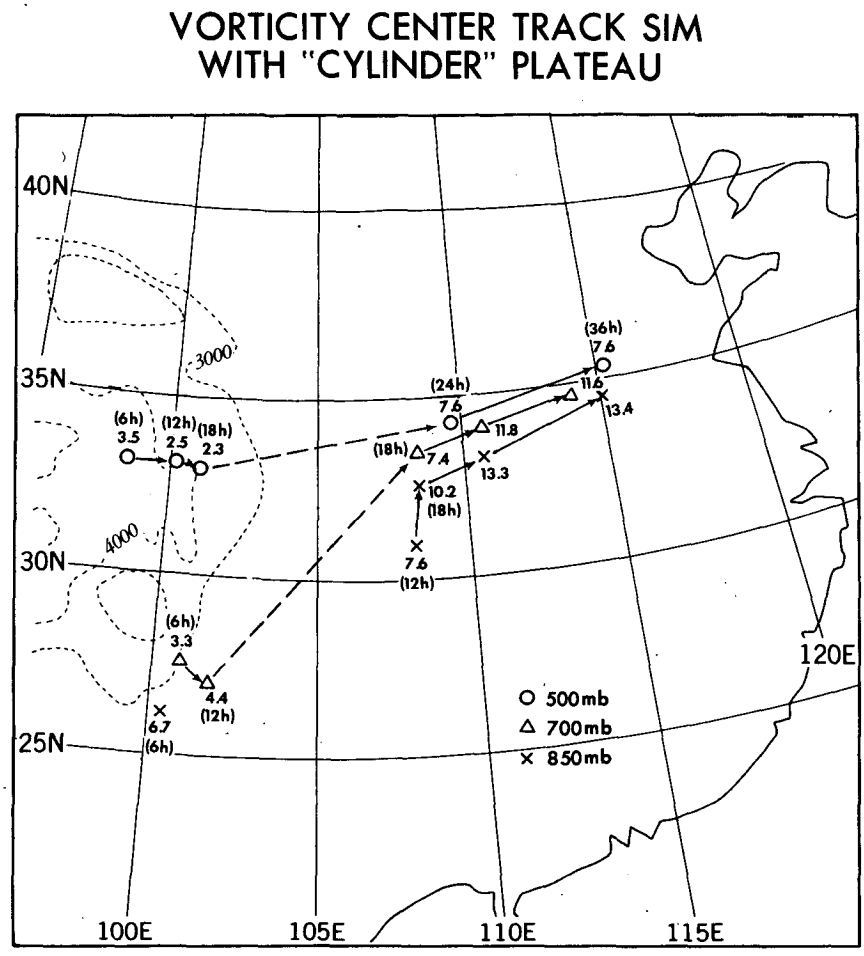

FIG. 20. Vorticity center tracks taken from the simulation with a "cylinder" plateau. Shadings as in Fig. 19.

similar to that of baroclinic instability modified by topography as described in Orlanski (1969).

After a careful examination, we rejected hypotheses B, C, and D in favor of hypothesis A. The major reasons are summarized as follows.

Both observed and simulated vortices are formed in the middle of a stagnation region which is located over the eastern flank of the plateau and resulted from the topographic blocking (see Figs. 12 and 18). The existence of this stagnation region, which is characterized by very weak horizontal motion, effectively eliminates local dynamical energy sources from the environmental flow, although the necessary conditions for barotropic instability near its southeast edge and for internal baroclinic instability around its northern top region may be satisfied. Besides, the presence of this stagnation region also significantly diminishes topographic generation of vorticity by reducing vortex stretching for the flow that moves over the plateau and by prohibiting convergence of the low-level confluent flow that moves around the terrain. In the absence of latent heating, the dynamic instability and/or the forcing due to the large-scale flow interacting with the Tibetan Plateau, by themselves, are not sufficient to generate the observed vortex.

On the other hand, the plateau blocking effect favors the establishment of an environment in which the air mass is potentially unstable to convection. A mesoscale boundary layer disturbance over the main body of the plateau is found to be responsible for triggering the vortex development. The simulation indicates a sudden onset of vigorous deep convection followed by an abrupt growth of the relative vorticity at 700 mb soon after the dynamic forcing associated with the triggering system moves into the western stagnation region. As far as the development mechanism is concerned, our principal result based upon the numerical experiments is that the warm SW vortex, together with associated heavy rainfall, is largely driven by convective latent heating and triggered by a middle tropospheric disturbance migrating eastward off the plateau. It is interesting to note that, in the absence of latent heating, the triggering disturbance attenuates gradually as it mi-

grates eastward; by the time it reaches the plateau boundary (3000 m isohypse), the dynamic forcing associated with this disturbance becomes too weak to initiate any intense deep convection. Thus the convective heating over the plateau appears to be significant for the initiation of the lee-side vortex, and the convective precipitation over the plateau seems to be a meaningful precursor to the genesis of the SW vortex. Because the thermal influences of the plateau contribute greatly to the convective activity over the plateau, they may indirectly but significantly affect the vortex formation in its earliest stage of development.

The present study focuses on the dynamics of the warm SW vortex, which are characterized by heavy precipitation and often are observed after the onset of the summer Indian monsoon. Although the case studied here may be representative, the conclusions derived based upon one particular case study have to be corroborated with other analyses and studies. The results derived from the simulation with a "cylinder" plateau suggest that the triggering mechanism for deep convection and vortex development may change when the background large-scale flow is altered. Apart from the disturbance over the main body of the plateau, convergence caused by the confluence of the two branches of flow on the lee side could also contribute to the triggering of active convection and vortex-genesis, if the confluent flows are strong enough. From a broader point of view, because the mesoscale forcing initiating these vortices is determined by the background large-scale circulation which is, in turn, substantially affected by the thermal and mechanical effects of the Tibetan Plateau, the genesis of the SW vortex may exhibit distinguishing characteristics for SW vortices occurring *before* the onset of the summer monsoon. This aspect of the SW vortices deserves further systematic and detailed research.

Acknowledgments. The authors are very grateful to Dr. B. B. Ross and Dr. G.-C. Lau for reading the manuscript and for the suggestions which improved the presentation of this paper, and to Mr. L. Polinsky for his assistance with the computations. Our appreciation also goes to Mr. W.-L. Li for providing the weather maps, to Mrs. J. Callan for typing the manuscript and to the GFDL drafting group for preparing the figures. One of the authors, B. Wang, is supported by NOAA/Princeton University Grant NA84EAD-00057.

REFERENCES

Chen, S.-J., and L. Dell'Osso, 1984: Numerical prediction of the heavy rainfall vortex over Eastern Asia monsoon region. *J. Meteor. Soc. Japan,* **62,** 730–747.

Gao, Y.-X., M.-G. Tang, S.-W. Luo, Z.-B. Shen and C. Li, 1981: Some aspects of recent research on the Qinghai-Xizang Plateau meteorology. *Bull. Amer. Meteor. Soc.,* **62,** 31–35.

Hovermale, J. B., 1983: Numerical experiments with the Sichuan flooding catastrophe (11–15 July 1981), *Proc. First Sino-American Workshop on Mountain Meteorology,* E. R. Reiter, B.-Z. Zhu and Y.-F. Qian, Eds. Science Press, 699 pp.

Luo, S.-W., 1979: Shearlines and vortices in the planetary boundary layer of Qinghai-Xizang Plateau, *Meteorology of Qinghai-Xizang (Tibet) Plateau,* T. C. Yeh and Y. X. Gao, Eds. Science Press, 278 pp. [in Chinese].

Manabe, S., J. Smagorinsky and R. F. Strickler, 1965: Simulated climatology of a general circulation model with a hydrologic cycle. *Mon. Wea. Rev.,* **93,** 769–798.

Mesinger, F., 1982: On the convergence and the error problems of the calculation of the pressure gradient force in Sigma coordinate models. *Geophys. Astrophys. Fluid Dyn.,* **19,** 105–117.

Orlanski, I., 1969: The influence of bottom topography on the stability of jets in a baroclinic fluid. *J. Atmos. Sci.,* **26,** 1216–1232.

——, and L. J. Polinsky, 1984: Predictability of mesoscale phenomena, *Mesoscale Observations and Very Short Range Forecasting, Nowcasting II. Proc., Second Int. Symp. on Nowcasting,* 3–7 September 1984, Norrkoping, Sweden, European Space Agency SP-208, Noordwijk, Netherlands, 271–280.

——, and B. B. Ross, 1984: The evolution of an observed cold front. Part II: Mesoscale Dynamics. *J. Atmos. Sci.,* **41,** 1669–1703.

Ross, B. B., 1986: The role of low-level convergence and latent heating in a simulation of observed squall line formation. Submitted to *Mon. Wea. Rev.*

——, and I. Orlanski, 1982: The evolution of a cold front. Part I: Numerical simulation. *J. Atmos. Sci.,* **39,** 296–327.

Smagorinsky, J., 1960: On the dynamical prediction of large-scale condensation by numerical methods. *Geophys. Monogr.,* No. 5, Amer. Geophys. Union, 71–78.

Tao, S.-Y., et al., 1980: *The Heavy Rainfalls in China,* Science Press, Beijing, 225 pp. [in Chinese].

Wang, B., 1987a: The nature of CISK in a generalized continuous model. *J. Atmos. Sci.* (in press).

——, 1987b: On the development mechanism for Tibetan Plateau warm vortices. *J. Atmos. Sci.* (in press).

Wu, G.-X., and S.-J. Chen, 1985: The effect of mechanical forcing on the formation of a mesoscale vortex. *Quart. J. Roy. Meteor. Soc.,* **111,** 1049–1070.

Yeh, T.-C. (Ye D. Z.), and Y.-X. Gao et al., 1979: The Meteorology of Qinghai-Xizang (Tibet) Plateau, Science Press, Beijing, 62–68. [in Chinese].